JCB Journal of Cell Biology

ARTICLE

# Alternative splicing of clathrin heavy chain contributes to the switch from coated pits to plaques

Gilles Moulay[1], Jeanne Lainé[1,2], Mégane Lemaître[3], Masayuki Nakamori[4], Ichizo Nishino[5], Ghislaine Caillol[6], Kamel Mamchaoui[1], Laura Julien[1], Florent Dingli[7], Damarys Loew[7], Marc Bitoun[1], Christophe Leterrier[6], Denis Furling[1]*, and Stéphane Vassilopoulos[1]*

**Clathrin function directly derives from its coat structure, and while endocytosis is mediated by clathrin-coated pits, large plaques contribute to cell adhesion. Here, we show that the alternative splicing of a single exon of the clathrin heavy chain gene (*CLTC* exon 31) helps determine the clathrin coat organization. Direct genetic control was demonstrated by forced *CLTC* exon 31 skipping in muscle cells that reverses the plasma membrane content from clathrin plaques to pits and by promoting exon inclusion that stimulated flat plaque assembly. Interestingly, mis-splicing of *CLTC* exon 31 found in the severe congenital form of myotonic dystrophy was associated with reduced plaques in patient myotubes. Moreover, forced exclusion of this exon in WT mice muscle induced structural disorganization and reduced force, highlighting the contribution of this splicing event for the maintenance of tissue homeostasis. This genetic control on clathrin assembly should influence the way we consider how plasticity in clathrin-coated structures is involved in muscle development and maintenance.**

## Introduction

Clathrin is recognized as a versatile molecule that mediates various functions as different as endocytosis and cell adhesion (Brodsky, 2012). This diversity of functions is based on the structure of the clathrin coats formed on the plasma membrane. The comparison between neurons and muscle fibers is an archetypal example of this structure–function relationship. While neurons produce small and calibrated clathrin-coated pits (CCPs) of short lifetimes, providing fast endocytosis kinetics (Royle and Lagnado, 2010; Kanaseki and Kadota, 1969; Saheki and De Camilli, 2012), clathrin polymerizes as flat plaques in differentiated muscle cells (Lampe et al., 2016; Vassilopoulos et al., 2014; Franck et al., 2019). These plaques are intimately associated with the cortical cytoskeleton and strongly adhere to their substrate through specific integrins (Vassilopoulos et al., 2014; De Deyne et al., 1998).

Clathrin molecules are composed of trimerized heavy chains (CHCs) with bound light chains that assemble to form a submembrane coat. Clathrin triskelia are recruited by clathrin adaptors that trigger clathrin-coated vesicle budding (McMahon and Boucrot, 2011; Robinson, 2004). The mechanism by which clathrin triskelia form different coated structures has been heavily debated, and two different models have been proposed for how CCPs grow (Heuser, 1980; Kirchhausen, 2009; Lampe et al., 2016). In the canonical model, clathrin triskelia adopt a puckered conformation, and the curvature of the cage reflects the curved shape of clathrin triskelia (Kirchhausen et al., 1986). The recruitment of cytosolic clathrin to the edge of a budding lattice by a nucleation-and-growth mechanism produces spherical clathrin coats, and curvature develops as a function of clathrin polymerization (Kirchhausen, 2009). In the constant area model, clathrin coats initially grow as flat hexagonal lattices that later remodel to form a coated invagination (Avinoam et al., 2015; Bucher et al., 2018; Heuser, 1980; Lampe et al., 2016). In large flat hexagonal lattices or "plaques" of clathrin, all leg segments are nearly coplanar. Although the different models are not mutually exclusive, no single model can explain

[1]Sorbonne Université, Institut National de la Santé et de la Recherche Médicale, Association Institut de Myologie, Centre de Recherche en Myologie, UMRS 974, Paris, France; [2]Sorbonne Université, Department of Physiology, Pitié-Salpêtrière Hospital, Paris, France; [3]Sorbonne Université, Institut National de la Santé et de la Recherche Médicale, Phénotypage du petit animal – UMS 28, Paris, France; [4]Department of Neurology, Osaka University Graduate School of Medicine, Osaka, Japan; [5]Department of Neuromuscular Research, National Institute of Neuroscience, National Center of Neurology and Psychiatry, Tokyo, Japan; [6]Aix Marseille Université, Centre National de la Recherche Scientifique, NeuroCyto, Marseille, France; [7]Institut Curie, PSL Research University, Centre de Recherche, Laboratoire de Spectrométrie de Masse Protéomique, Paris, France.

*D. Furling and S. Vassilopoulos contributed equally to this paper; Correspondence to Stéphane Vassilopoulos: s.vassilopoulos@institut-myologie.org; Denis Furling: denis.furling@sorbonne-universite.fr.

the diversity of endocytic clathrin-coated structures observed in cells. Why clathrin is assembling flat in some cell types while it directly generates curved coated pits in others and how this plasticity is regulated are unknown.

Membrane-trafficking genes are developmentally and tissue-specifically regulated by alternative splicing (Dillman et al., 2013; Giudice et al., 2014). In particular, conserved alternative splicing events in the brain and skeletal muscle take place in genes encoding endocytosis proteins (Merkin et al., 2012), and their regulation during development to ensure transition from fetal to adult isoforms is controlled by RNA splicing factors from CELF and MBNL families (Brodsky, 2012; Fugier et al., 2011). It has recently been shown that exon 31 (ex31) of the *CLTC* gene encoding the CHC is included by alternative splicing during mouse muscle maturation (Giudice et al., 2016). Here, we investigated the role of this alternatively spliced exon and showed that developmentally regulated inclusion of exon 31 encoding a seven–amino acid sequence within the trimerization domain of CHC contributes to the presence of clathrin plaques. By modulating the splicing of endogenous *CLTC* exon 31, we demonstrated that its inclusion participates in the formation of plaques in cells usually devoid of them, and inversely, its exclusion strongly reduces plaque formation in myotubes. Interestingly, the abnormal *CLTC* exon 31 exclusion found in congenital myotonic dystrophy type 1 (cDM1) was associated with reduced plaque formation in patient myotubes and correlated with disease severity. Finally, forced exon 31 skipping in the muscles of mice impaired muscle architecture and force generation. Altogether, our results highlight the role of seven amino acids regulated by the alternative splicing of *CLTC* exon 31 in clathrin's fate to form either CCPs essential for fast endocytosis or plaques that are required for appropriate muscle development and function.

## Results

### CHC exon 31 alternative splicing correlates with clathrin coat diversity

We initially compared the different types of clathrin-coated structures present at the surface of neurons and muscle cells. Super-resolution light microscopy showed that neurons and undifferentiated myoblasts produce diffraction-limited fluorescent puncta corresponding to individual coated pits positive for both CHC and its plasma membrane (PM) adaptor protein AP2, whereas differentiated myotubes exhibit larger clathrin patches (Fig. 1 A and Fig. S1 A). We unroofed cultured neurons, myoblasts, or myotubes using ultrasonication to access the cytoplasmic side of the PM and to directly compare the different types of clathrin-coated structures produced using platinum-replica EM (PREM). Neurons formed exclusively small, extremely calibrated (60–80 nm in diameter) CCPs in the soma, synaptic boutons, and axons, but they did not form flat clathrin assemblies (Fig. 1, B–E). Similarly, other cell types, such as human induced pluripotent stem cells (iPSCs) and BS-C-1 cells, formed exclusively spherical coated pits, whereas HeLa cells formed both spherical coated pits and some flat clathrin lattices (FCLs) as previously reported (Boucrot et al., 2010; Sochacki and Taraska, 2019; Grove et al., 2014; Fig. S1, B–D). Whereas myoblasts exhibited CCPs with a larger diameter (>100 nm) compared with neurons (Fig. 1 F), a drastic change occurred during myogenic differentiation associated with the transition of myoblasts into myotubes. In contrast to myoblasts, myotubes formed large flat clathrin plaques covering significant portions of the PM (purple-colored in Fig. 1 G). At the functional level, this morphological change occurring during the differentiation of myoblasts was associated with reduced clathrin-mediated endocytosis (CME) activity measured by transferrin uptake assay between myoblasts and myotubes (Fig. 1 H; and Fig. S1, F and G). Of note, although CCPs are the main clathrin structures encountered in myoblasts, some FCLs are present, albeit at much a lower frequency (Fig. S1 E); conversely, myotubes displaying mostly large clathrin plaques still produce canonical coated pits and are capable of performing endocytosis, as small puncta are visible using super-resolution light microscopy (Fig. 1 A). The drastic modification of clathrin assembly occurred independently of a change in clathrin protein levels (both heavy and light chains; Fig. S2 A), although an increase in AP2 protein content was detected in agreement with a recent report showing that an AP2 level increase contributes to the formation of large clathrin structures (Dambournet et al., 2018).

Since it has been shown that exon 31 of the *CLTC* gene encoding the CHC is included by alternative splicing during mouse muscle maturation (Giudice et al., 2016), we examined whether this splicing switch could act as a genetic signal controlling the type of clathrin structures formed at the cell surface. We show that the regulation of *CLTC*-ex31 is conserved in human muscle tissue with a progressive inclusion of this exon during development, which becomes the main isoform in the latest stage of fetal development (Fig. 1 I). The immature clathrin isoform, excluding *CLTC*-ex31, is the only form expressed in various cell types that produce exclusively CCPs, such as neuronal cultures, iPSCs, and BS-C-1 cells (Fig. 1, B–E; and Fig. S1, B and C). Conversely, cells displaying clathrin plaques show increased *CLTC*-ex31 inclusion. A modest inclusion was evidenced for HeLa cells, which displayed some FCLs upon PREM analysis (Fig. S1 D). Moreover, the formation of plaques was strongly associated with *CLTC*-ex31 inclusion observed during the differentiation of iPSCs and myoblasts into myotubes that produced abundant large lattices and FCLs (Fig. 1, G and I). The exon inclusion observed by reverse transcription PCR (RT-PCR) was also confirmed in publicly available transcriptome data from in vitro myogenic differentiation (Fig. S2 B; Trapnell et al., 2014); however, exon 31 inclusion is not currently documented at the protein level in proteomic or crystallography databases.

We therefore performed a shotgun proteomic analysis enabling the detection of unique peptides covering the exon junctions with or without exon 31 in our myogenic differentiation model (Fig. S2, C and D). Quantifying the relative amounts of peptides ± exon 31 confirmed the RT-PCR results at the protein level (Fig. 1 I), with a replacement of CHC protein without exon 31 by CHC protein including exon 31 during human muscle cell differentiation (Fig. 1 J). Altogether, our results reveal a correlation between the alternative splicing of exon 31 and the structural organization of clathrin, with exon inclusion associated with plaques and exclusion associated with pits.

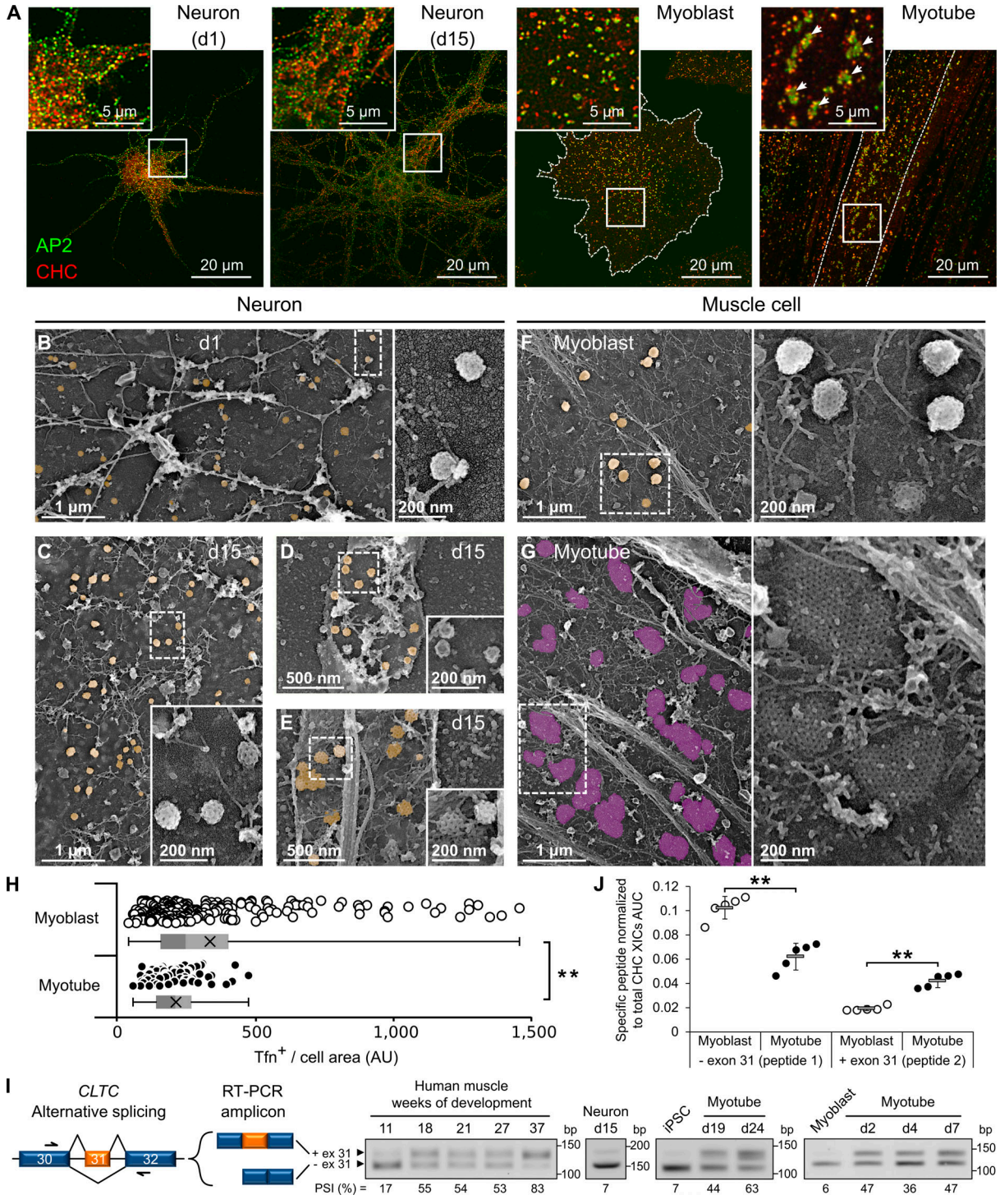


Figure 1. **Clathrin coat diversity correlates with *CLTC* exon 31 splicing. (A)** Super-resolution imaging of the ventral PM from representative rat neurons at 1 or 15 d of culture (d1; d15) and human myoblasts and myotubes (differentiated for 11 d). CHC immunofluorescent staining in red and adaptor protein 2 (AP2) staining in green. Insets presented at the same magnification, with arrows showing clathrin plaques. **(B–G)** High-magnification transmission EM views of unroofed rat neurons and human muscle cells. CCPs are shown in yellow, and plaques are shown in purple, with native grayscale kept in magnification insets. **(B)** Unroofed soma of d1 rat neurons. **(C–E)** d15 rat neurons with unroofed soma (C), synaptic bouton (D), and axon (E). **(F)** Human myoblast. **(G)** Human myotubes differentiated for 11 d. All images are presented at the same 1-µm scale for comparison, with the exception of D and E, which have 500-nm scale bars. All magnification insets are shown at the same scale and are outlined with dashed rectangles in each image. **(H)** Fluorescent transferrin (Tfn) uptake normalized to cell area, measured in human myoblasts or myotubes differentiated for 8 d. Box plots show median extended from 25th to 75th percentiles, minimum and maximum data point whiskers, and average cross (myoblasts, $n = 234$; myotubes, $n = 73$; **, $P \leq 0.005$). **(I)** Schematic of CHC exon 31 alternative splicing (exon of 21 nucleotides numbered based on National Center for Biotechnology Information mouse RNA reference sequence NM_001356393.1 from GenBank). Arrows indicate RT-PCR primer positions in bordering constitutive exons (in blue), with expected RT-PCR amplicons shown on the right with or without the inclusion of alternative exon 31 (in orange). The RT-PCR electrophoresis presents *CLTC* exon 31 alternative splicing in d15 rat neurons as well as

human muscles at different developmental stages and human myotubes differentiated from iPSCs or myoblasts for up to 24 and 7 d, respectively. PSI densitometric quantifications are shown below. **(J)** Quantification of CHC isoforms by label-free MS analysis. Total CHC protein was immunopurified from human myoblasts or myotubes differentiated for 4 d and digested by Glu-C (see Fig. S2). Peptides 1 and 2 specific to CHC isoforms ± exon 31 were quantified by measuring the area under the curve (AUC) of XICs. Means ± SD with $n = 5$ (**, $P \leq 0.005$ for myoblast versus myotube with both peptides). AU, arbitrary unit.

### *CLTC* exon 31 skipping induces CCP formation

To demonstrate a role for *CLTC*-ex31 alternative splicing on plaque versus pit formation, we developed an exon skipping strategy to reverse this splicing event in myotubes by promoting *CLTC*-ex31 exclusion (Fig. 2). We designed an exon skipping antisense sequence within the optimized U7–small nuclear RNA system (Goyenvalle, 2012) packaged into an adeno-associated vector (AAV-U7-CLTCex31). As a consequence, the *CLTC* mRNA isoform containing exon 31 switched from 50% to 17% in skipped myotubes (Fig. 2 A) without changes in CHC, clathrin light chain A (CLCa), and adaptors α-AP2 or PICALM protein levels or in binding between CHC and CLCa proteins (Fig. 2 B and Fig. S4, A, B, and D). Visualization of clathrin ultrastructure by PREM showed that *CLTC*-ex31 skipping correlated with a reduction in the number and size of plaques for the benefit of pit formation (Fig. 2, C and D).

We performed a morphometric analysis in which clathrin structures present on PREM images were plotted according to their area and curvature (Fig. 2 E). We defined an area cutoff threshold of 40,000 $nm^2$ corresponding to the size of the largest CCPs encountered with diameters of ∼200 nm, while a curvature threshold was set manually to segregate FCLs from CCPs in control myotubes after measuring each structure's electron opacity, as described in Fig. S3 A. It is worth noting that we chose to use the term FCL to describe flat structures comprising both small objects below the area threshold and big and flat structures corresponding to clathrin plaques above this threshold and found in the lower-right quadrant. This analysis revealed that the relative frequency of CCPs in the upper-left quadrant increased from 23% in control myotubes to 40% in the skipped ones, while the size of CCPs remained unchanged (Fig. 2, E and F). The relative number of objects in the lower-left quadrant was not impacted by exon skipping. Interestingly, promoting the exclusion of exon 31 in differentiated myotubes increased endocytic pits of large size (upper-right quadrant). Upon *CLTC*-ex31 skipping, the amount of clathrin plaques was lowered from 39% to 17% (Fig. 2 E) and their density decreased while the CCP density increased (Fig. 2 G). Moreover, the structural changes toward pit formation translated into a functional switch, as excluding *CLTC*-ex31 led to increased CME in skipped human and murine myotubes (Fig. 2 H and Fig. S4, C and E–H). These results demonstrate that CHC devoid of exon 31 favors the assembly of curved structures at the expense of clathrin plaques.

### *CLTC* exon 31 inclusion contributes to plaque formation

To further confirm the contribution of *CLTC*-ex31 in the formation of clathrin plaques, we included *CLTC*-ex31 in cells that mainly displayed CCPs. Because CELF1 splicing factor has been shown to regulate *CLTC*-ex31 alternative splicing during striated muscle development (Blue et al., 2018), we took advantage of this regulation to promote *CLTC*-ex31 inclusion in myoblasts following siRNA-mediated CELF depletion (Fig. 3 A). As a consequence, we observed an increase in flat clathrin coat assembly at the surface of myoblasts, including exon 31, and fewer CCPs budding compared with control myoblasts (Fig. 3 B). A detailed morphometric analysis of PREM images revealed an increase in FCLs following *CLTC*-ex31 inclusion composed of both small flat structures (lower-left quadrant of the dot plot) and large clathrin-coated plaques (Fig. 3 C), an intermediate phenotype between that of a myoblast and a myotube. Exon 31 inclusion also had the opposite effect to exon skipping by reducing large endocytic pit numbers. However, we observed in this experimental procedure that the upper frequency plot was shifted toward smaller structures (Fig. 3 C), likely because *CLTC*-ex31 inclusion is not the sole splicing event misregulated by CELF depletion. Overall, in agreement with our previous observation that exon 31 depletion leads to decreased amounts of plaques, the formation of flat assemblies seems to be associated with *CLTC*-ex31 inclusion.

### Structural in silico analysis provides a model for triskelion curvature

Exon 31 is of particular interest from a structural standpoint because it is located in a helical tripod belonging to the clathrin C-terminal trimerization domain (Fig. 4 A; Näthke et al., 1992). Although all available clathrin structures are based on brain isolates or are from cell types that do not express *CLTC*-ex31 (Fotin et al., 2004; Wilbur et al., 2010; Ybe et al., 2013), we could model the consequences of exon 31 inclusion in silico (Fig. 4, B–E). The protein sequence belonging to the tripod domain was conserved in mammals, with and without exon 31. Inclusion of the seven residues encoded by exon 31 is predicted to maintain an α-helix secondary structure (Jones, 1999), with a helix strengthened by several new potential salt bridges (Fig. 4 B). Modeling both α-helices showed a rotation of the C-terminus in the inclusion isoform as well as the lengthening of a hydrophobic stretch (Fig. 4 C). Helical wheel representations further revealed that residues from exon 31 did participate in both the strengthening of a hydrophobic face on one side of the helix (V14 and I17) and the disruption of a smaller stretch on the other side by charged residue E19 (Fig. 4 C). The amphiphilicity, which is the opposition of polar and nonpolar faces oriented along the long axis of the α-helix, was therefore increased by exon 31 inclusion, as confirmed by calculating the helical hydrophobic moments (Fig. 4 D). Lastly, we predicted that the α-helix propensity to form coiled-coil regions was strikingly increased around exon 31 (Fig. 4 E). Thus, these data support a model in which the tripod quaternary structure is strengthened by exon 31–related increase of coiled-coil interactions between the three α-helices of the trimerization domain.

### *CLTC* exon 31 misregulation in myotonic dystrophy disease

Alternative splicing misregulations have been shown to play a central role in myotonic dystrophy type 1 (DM1) pathophysiology

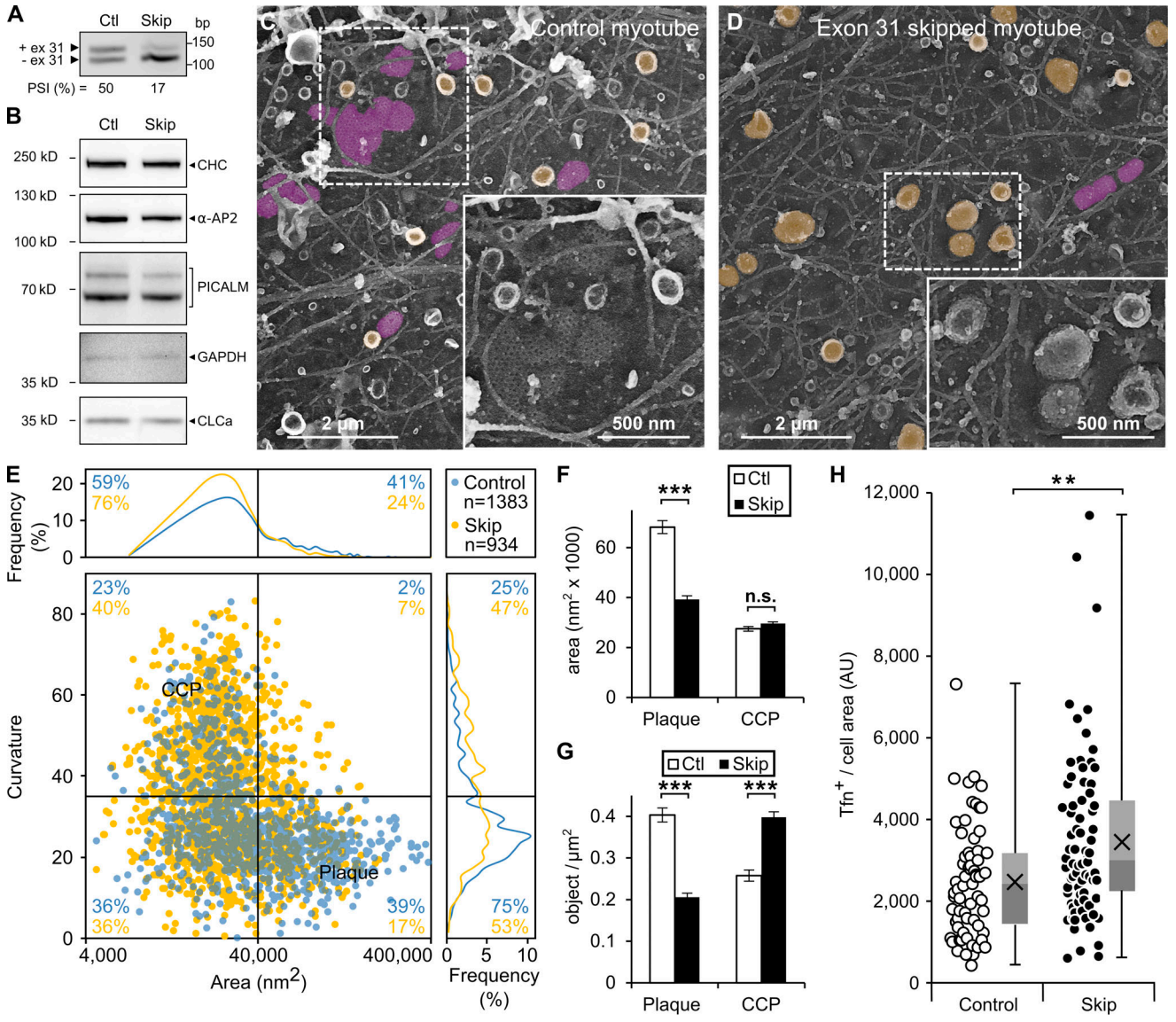


Figure 2. **CHC exon 31 skipping favors CCP formation. (A–H)** In vitro *CLTC*-ex31 skipping induced at 3 d of differentiation in normal human myotubes by AAV-U7-CLTCex31 vector transduction, followed by analysis 5 d later. **(A)** *CLTC*-ex31 RT-PCR. Ctl, control nontransduced myotubes; Skip, AAV transduced myotubes. **(B)** Western blot. PICALM, phosphatidylinositol-binding clathrin assembly protein; α-AP2, adaptor protein 2 subunit α. **(C and D)** Representative electron micrographs of the ventral PM of a Ctl and a myotube transduced to promote *CLTC*-ex31 skipping. CCPs and plaques are shown in yellow and purple, respectively, with native grayscale kept in magnified insets. **(E)** Dot plot morphometric analysis of the distribution of clathrin-coated structures along curvature and size (area) as described in Fig. S3 A. The percentages of objects counted in each quadrant are reported in blue for control myotubes and orange for exon 31 skipped myotubes. **(F)** Mean area of clathrin structures classified as plaque and CCP. Control, $n$ = 1,383; Skip, $n$ = 934; ***, P ≤ 0.0001 for plaques; P = 0.1759 for CCP; SEM bars. n.s., nonsignificant. **(G)** Plaque and CCP mean density per micrometer squared of myotube PM, with SEM bars (Control, $n$ = 50; Skip, $n$ = 66; ***, P ≤ 0.0001 for plaques; ***, P ≤ 0.0001 for CCP). **(H)** Transferrin uptake assay. Box plots show median extended from 25th to 75th percentiles, minimum and maximum data point whiskers, and average cross (Control, $n$ = 66; Skip, $n$ = 78; **, P ≤ 0.005). Tfn, fluorescent transferrin. AU, arbitrary unit.

(Sznajder and Swanson, 2019). We examined the *CLTC*-ex31 profile in skeletal muscle biopsies of a well-characterized cohort of DM1 patients suffering from the cDM1 form (Nakamori et al., 2017). We found that *CLTC*-ex31 was mis-spliced in several cDM1 patients with an abnormal *CLTC*-ex31 exclusion compared with control age-matched spinal muscular atrophy (SMA) patients who presented a normal pattern of *CLTC*-ex31 inclusion (Fig. 5 A). We further observed a correlative trend between *CLTC*-ex31 exclusion and the severity of the disease by plotting each percent spliced-in (PSI) value against its corresponding biopsy histological grade (Fig. 5 B). A similar abnormal *CLTC*-ex31 exclusion was confirmed in myotubes derived from a DM1 child suffering from a severe form of the disease compared with control myotubes derived from an age-matched nonaffected control (CTL) individual (Fig. 5 C).

Next, we investigated the organization of clathrin-coated structures by PREM in DM1 myotubes presenting smaller plaques and more pits compared with CTL myotubes (Fig. 5, D and E). We found a half fewer clathrin plaques in DM1 (22% versus 44% in CTL) along with a concomitant increase in CCPs (53%

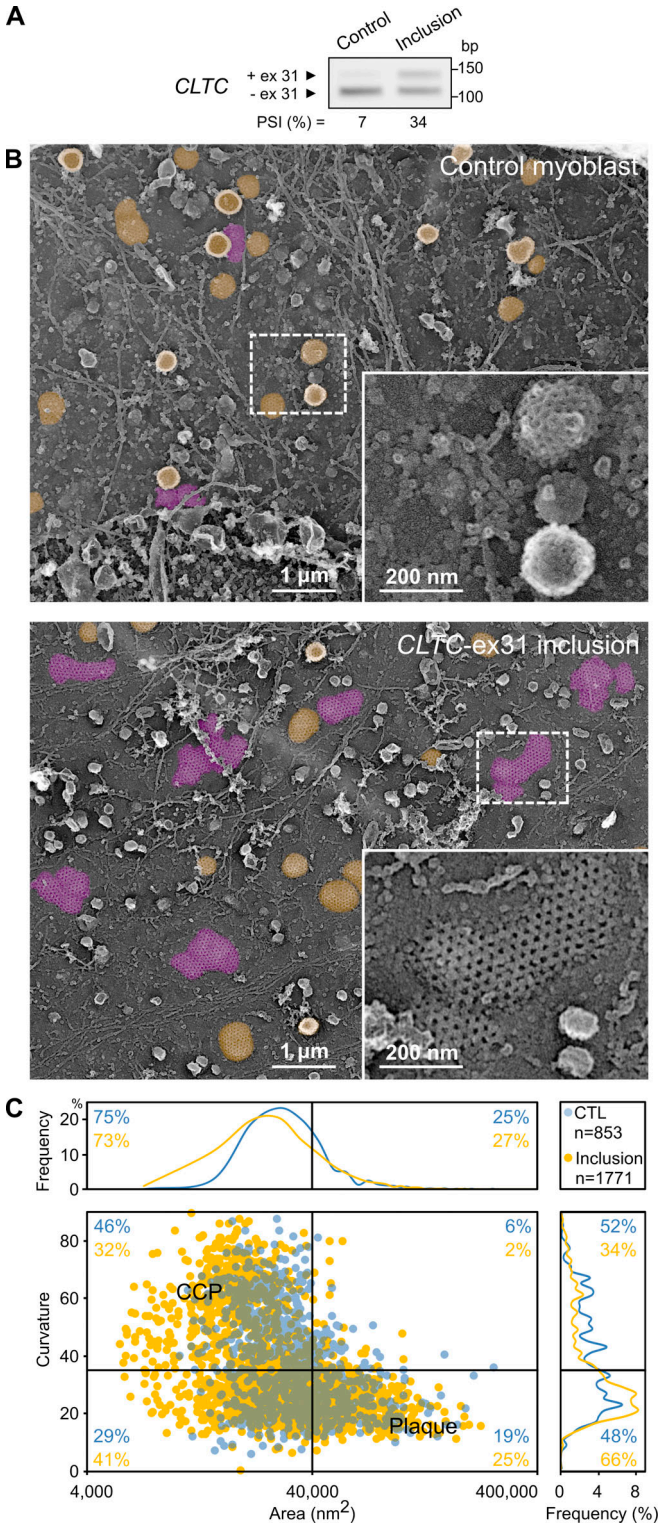


Figure 3. **The inclusion of clathrin exon 31 contributes to plaque formation. (A)** *CLTC*-ex31 RT-PCR analysis of human control myoblasts (transfected by a control siRNA) and myoblasts in which exon 31 inclusion was induced by siRNA-mediated CELF depletion. **(B)** Representative electron micrographs of the ventral PM of human control myoblasts or myoblasts including *CLTC* exon 31. CCP and plaque structures are shown in yellow and purple, respectively, with native grayscale kept in magnified insets. **(C)** Dot plot morphometric analysis of the clathrin-coated structures.

versus 33% in CTL; Fig. 5 F), which phenocopied the experimental skipping of *CLTC*-ex31 on control myotubes. Similar to experimental exon skipping, the DM1 myotubes exhibited a comparable frequency of small and flat clathrin structures (lower-left quadrant) but had less impact on the rare population of endocytic pits of large size (upper-right quadrant). Additional analysis confirmed that plaques were smaller and less numerous per surface unit in DM1 myotubes, while CCPs of comparable size were denser on DM1 sarcolemma compared with CTL (Fig. 5, G and H). Functionally, we observed increased CME activity in DM1 myotubes compared with CTL myotubes (Fig. 5, I–K). Thus, clathrin-coated structures in DM1 myotubes displayed a myoblast-like immature phenotype with an abundance of CCPs and increased endocytosis activity.

### Forced *Cltc* exon 31 skipping compromises muscle structure and function

We next determined the effect of specifically removing exon 31 from clathrin on muscle structure and function. We depleted this isoform in tibialis anterior (TA) muscles of adult wild-type mice transduced with the AAV-U7-CLTCex31 vector to achieve in vivo exon skipping (Fig. 6 A). Intramuscular vector injections resulted in dose-dependent skipping of *Cltc*-ex31, and we could reliably achieve >70% skipping at 1 and 2 mo after injection when muscle histology and function were evaluated (Fig. 6 B and Fig. S5, A and B), without changes in CHC protein amount or its associated light chain CLCa upon coimmunoprecipitation (Fig. S5 C). While histological analysis displayed no gross alterations (Fig. 6, C and D; and Fig. S5 D), increased muscle mass was measured at 2 mo after injection (Fig. 6 E). EM revealed that depletion of the clathrin isoform containing exon 31 led to structural alterations of muscle fibers, presenting detachment of the contractile apparatus from the PM (Fig. 6 G) or circumferential subsarcolemmal disorganizations reminiscent of ringed fibers in which the contractile apparatus appears longitudinal on muscle cross sections (Fig. 6 H). In addition, a significant impact of *Cltc*-ex31 skipping on muscle function was revealed by the reduction of force production at both time points and an increased muscle relaxation time following tetanic stimulation 1 mo after injection (Fig. 6, I–L). We observed that the exclusion of exon 31 rendered the muscle more sensitive to eccentric exercise, an index of muscle fragility, as a drop of the force generated by the AAV-injected muscles relative to the control contralateral muscles was measured after repeated eccentric contractions (Fig. S5 E). These results suggest that the seven–amino acid stretch within the clathrin trimerization domain is required for the maintenance of muscle homeostasis.

## Discussion

In this study, we directly assessed the link between the alternative splicing of CHC (*CLTC*) exon 31 and the diversity of clathrin structures present at the PM. We showed that different cell types produce different kinds of clathrin structures, and our results suggest that the capacity to form plaques increases with the inclusion of exon 31 in the CHC isoform (*CLTC*-ex31). Neurons, iPSCs, and BS-C-1 cells that are all well known for

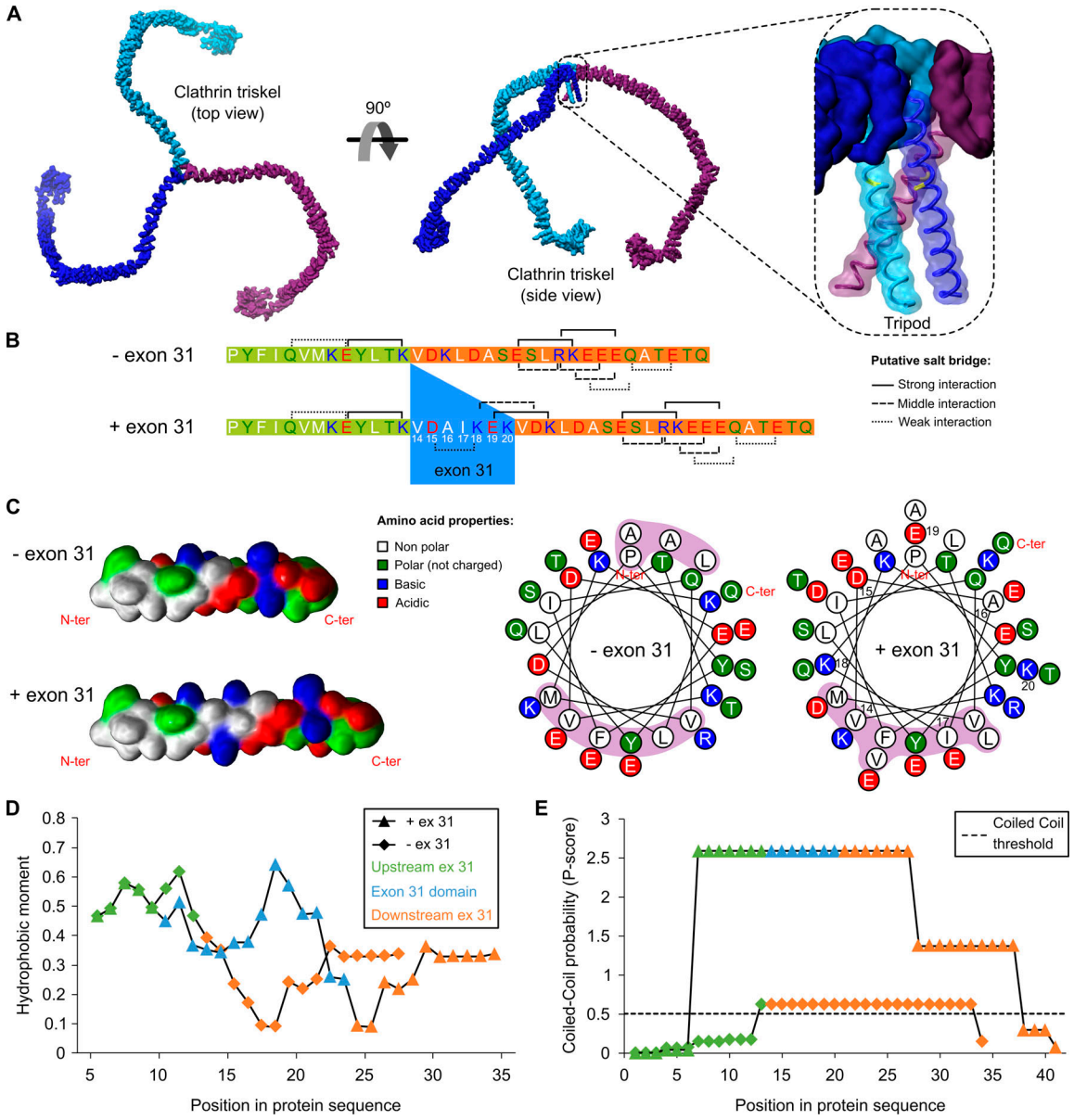


Figure 4. **Clathrin isoform structural model and in silico analysis. (A)** CHC trimer (or triskelion) rendered from two viewpoints. Clathrin monomers are shown in purple, light blue, and dark blue. A magnification of the C-terminal trimerization domain is shown on the right. This structure does not possess exon 31, and the junction site of exon 30 and exon 32 is highlighted in yellow in each magnified α-helix forming the tripod. **(B)** Amino acid sequence of the two alternative splicing isoforms of the CHC C-terminal α-helix. On top, a monomer α-helix formed of exon 30 in green and exon 32 in orange is shown. The sequence below shows the alternative splicing isoform with the inclusion of exon 31 highlighted in blue. Amino acids are presented in one-letter code and colored by properties. Potential *i*, *i* + 4 and *i*, *i* + 3 intrahelical ionic interactions are shown as brackets above and below each sequence, respectively. **(C)** Secondary structures of the two isoforms. The structures shown on the left were 3D modeled and surface rendered as canonical α-helices. The helical wheel representation of each helix is shown on the right, with residues pertaining to exon 31 numbered from 14 to 20, as in B. Non-polar regions are highlighted in purple. C-ter, C terminal; N-ter, N terminal. **(D)** Hydrophobic moments calculated along the α-helix over 11 residues with a one-residue increment. **(E)** Prediction of the tripod quaternary structure assembly by calculating coiled-coil interaction probability in the presence or absence of exon 31.

producing exclusively coated pits at their surface have little to no expression of *CLTC*-ex31. In contrast, myotubes that form plaques expressed the *CLTC*-ex31 inclusion isoform. We showed by in silico analysis that inclusion of exon 31 adds seven amino acids that extend and maintain secondary α-helices involved in the tripod structure of clathrin's trimerization domain. As a result, the helices' amphiphilicity was increased along with their potency to form coiled-coil interactions, which we predicted could reduce the clathrin triskelion tripod angle, increase the pucker angle, and lead to the flattening of individual triskelia and participation in clathrin plaque formation.

We validated the hypothesis that exon 31 participates in clathrin plaque formation by modulating its splicing in a muscle cell model. Indeed, skipping exon 31 in myotubes resulted in less plaque production along with an increase in coated pits and endocytic activity, whereas exon 31 inclusion through inhibition

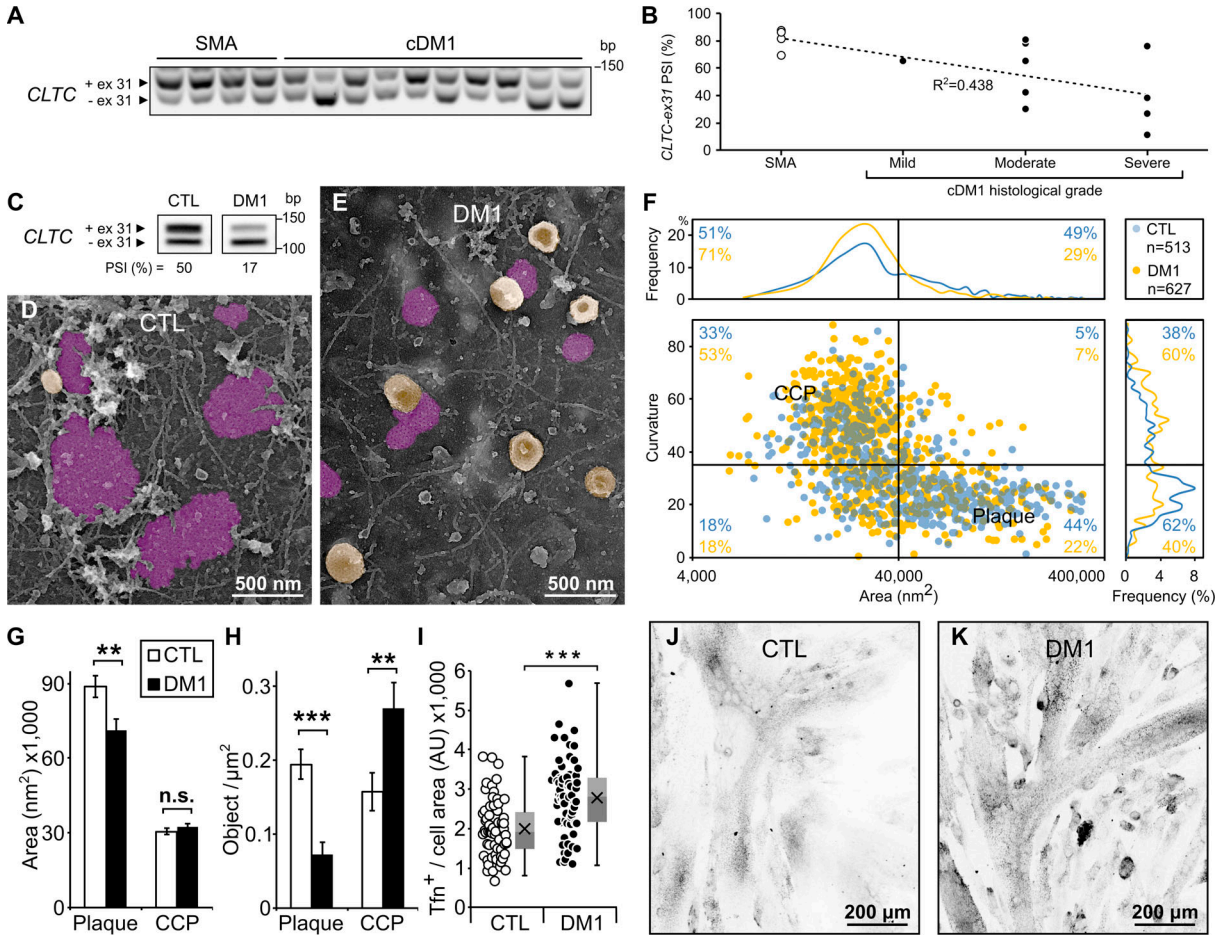


Figure 5. **Misregulated *CLTC*-ex31 splicing in DM1 disease. (A)** RT-PCR analysis of *CLTC* exon 31 alternative splicing in human skeletal muscle samples from control SMA and cDM1 infants. **(B)** PSI densitometric quantification of RT-PCR lanes presented in A plotted against corresponding muscle histological severity grade. **(C–I)** Analysis of human myotubes differentiated for 4 d in vitro from CTL or DM1 immortalized myoblast cells. **(C)** RT-PCR of *CLTC* exon 31 (panels for each event come from the same gel). **(D and E)** Representative electron micrographs of the ventral PM of CTL and DM1 cells. CCPs and plaques are shown in yellow and purple, respectively. **(F)** Dot plot morphometric analysis of clathrin-coated structures at the CTL and DM1 myotube PMs. **(G)** Mean area of clathrin structures classified as plaque (**, P ≤ 0.005) and CCP (P = 0.3621). CTL, *n* = 513, and DM1, *n* = 627; SEM bars. n.s., nonsignificant. **(H)** Plaque and CCP mean density per micrometer squared of myotube PM, with SEM bars (CTL, *n* = 37; DM1, *n* = 42; ***, P ≤ 0.0001 for plaque; **, P ≤ 0.005 for CCP). **(I)** Transferrin uptake assay in CTL and DM1 myotubes. Box plots show median extended from the 25th to 75th percentiles, minimum and maximum data point whiskers, and average cross (CTL, *n* = 63; DM1, *n* = 68; ***, P ≤ 0.0001). Tfn, fluorescent transferrin. **(J and K)** Representative images of transferrin uptake in CTL and DM1 myotubes quantified in I. AU, arbitrary unit.

of CELF splicing factors in myoblasts promoted increased clathrin flat assembly. Thus, we propose that clathrin is genetically programmed and regulated to produce two conformations of the heavy chain, a ubiquitous form (i.e., the neuronal isoform) and a tissue-specific and developmentally regulated flatter version (i.e., the *CLTC*-ex31 muscle isoform).

Our work shows the existence of two different isoforms of clathrin's trimerization domain, which is in agreement with previous simulations with a model of clathrin self-assembly suggesting two conformations: a nearly planar one found in plaques and a curved conformation found in cages, both depending on the clathrin triskelion pucker angle (den Otter and Briels, 2011). Thus, it is tempting to propose that clathrin molecules containing the seven additional amino acids of exon 31 produce planar triskelia and those without it produce puckered triskelia.

An important consequence of this hypothesis concerns the composition of individual triskelia with either zero, one, two, or three exon 31-containing CHCs. According to the relative abundance of the two spliced variants, different cell types will retain a relative fraction of triskelia with varying amounts of each isoform. Except in extreme situations such as in myotubes, where a majority of clathrin molecules contain exon 31, the probability of obtaining triskelia purely composed of heavy chains containing exon 31 in other cell types (such as HeLa cells, which are capable of forming plaques) is much lower. Thus, composite triskelia heterotrimers with one or two exon 31-containing CHCs may already favor or trigger flat assembly, suggesting a dominant effect.

While our results point toward a direct effect of the seven amino acids encoded by *CLTC* exon 31 on lattice structure, we cannot exclude that they could also modify the interaction with

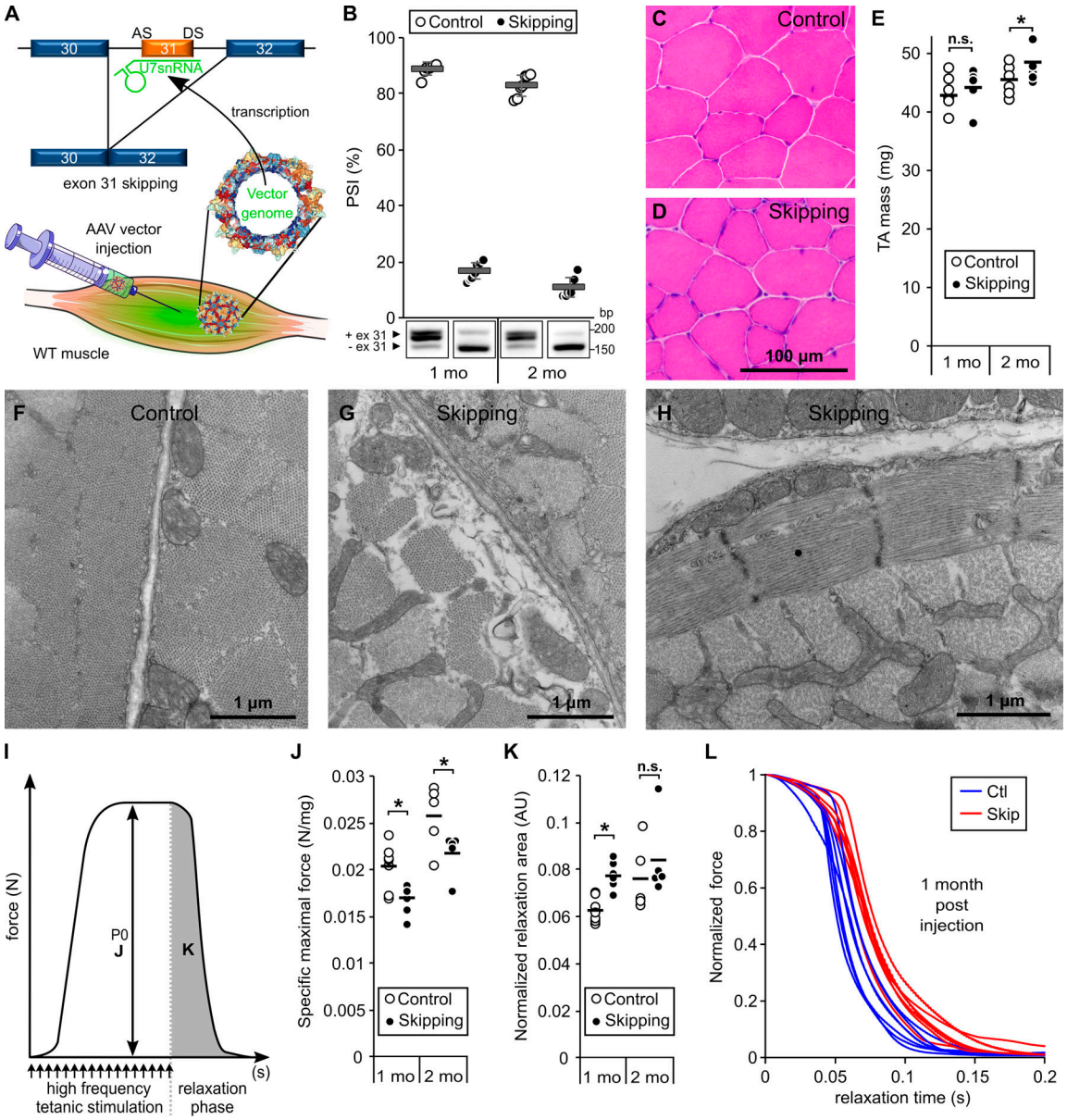


Figure 6. **Consequences of forced *Cltc* exon 31 skipping in vivo. (A)** Illustration of the exon skipping strategy. The AAV-U7-CLTCex31 vector is injected in the TA muscle with saline injection in the contralateral muscle. The vg are delivered to the nuclei of muscle fibers, where they are transcribed into modified U7 small nucleolar RNAs containing an antisense sequence covering both the splicing donor sequence (DS) and the acceptor sequence (AS) surrounding exon 31. This specific binding to *Cltc* premessenger RNA competes with the spliceosomal machinery and inhibits exon 31 splicing, which provokes its skipping in the mRNA. Blue boxes represent constitutive exons and the orange box represents alternative exon 31. **(B)** RT-PCR validation of in vivo *Cltc* exon 31 skipping 1 or 2 mo after AAV-U7-CLTCex31 intramuscular administration. Quantifications showing average PSI and SEM are shown on top of representative mice electrophoretic profiles (1-mo panels and 2-mo panels come from the same gels; see Fig. S5 B). Control saline injection data points are shown in white and skipped muscle in black ($n$ = 6, 7, 7, and 6 from left to right). **(C and D)** Representative hematoxylin and eosin staining on TA muscle transversal sections 2 mo PI; see also Fig. S5 C for staining at 1 mo PI. Images in C and D are at the same magnification. **(E)** Mean mass of the treated TA muscles at 1 mo ($n$ = 7, n.s.) or 2 mo PI ($n$ = 6; *, P ≤ 0.05). **(F–H)** Representative electron micrographs of a control muscle cross section (F) compared with the ultrastructural phenotypes encountered in G and H following muscle exon 31 skipping. **(I)** Schematic representation of a typical myogram tracing collected following tetanic stimulation of isolated TA muscle. **(J)** Mean specific maximal force in treated and control muscles corresponding to P0 in illustration I, at 1 mo ($n$ = 7; *, P ≤ 0.05) or 2 mo PI ($n$ = 5; *, P ≤ 0.05). **(K)** Quantification of average relaxation phases (once stimulation is discontinued), corresponding to the gray area illustrated in I, at 1 mo ($n$ = 7; *, P ≤ 0.05) and 2 mo PI ($n$ = 5; P = 0.0625). **(L)** Myograms of the force-normalized relaxation phases corresponding to mean quantifications at 1 mo PI in J. Control and skipped muscles are shown as blue and red curves, respectively ($n$ = 5 mice). AU, arbitrary unit; n.s., nonsignificant.

clathrin adaptors. In the dominant effect scenario in which exon 31-containing heavy chains coassemble with exon 31-skipped heavy chains, the mixed coil-coiled region could be altered in a way that recruits different clathrin adaptors or reduces binding to curvature generators. Future work on the precise composition of triskelia in the context of exon 31 alternative splicing could shed light on the mechanism by which heterotrimers promote flat assembly. Our results suggest that the exon 31 inclusion

threshold to obtain plaques is rather low (5–20%) and that approaching 50% exon 31 inclusion strongly favors the ratio of plaques over CCPs.

While there is a strong correlation between exon 31 inclusion and clathrin plaque formation, the data presented here do not deal with possible shape transitions during vesicle budding nor do they explain how a flat lattice can be shaped into a curved vesicle. Several other determinants can affect the assembly of clathrin structures at the PM, which could explain why myotubes are also capable of forming canonical coated pits and how clathrin plaques remodel to produce coated pits budding at their periphery (Lampe et al., 2016). As previously reported, increased AP2 expression in fibroblasts was associated with increased clathrin plaques (Dambournet et al., 2018). Similarly, increased expression of the Dab2 adaptor in Cos7 cells (Chetrit et al., 2009) and BS-C-1 cells (Mettlen et al., 2010), as well as PICALM depletion (Meyerholz et al., 2005), also resulted in increased FCL formation. Thus, a modification of adaptor concentration could directly contribute to shift the balance between CCPs and clathrin plaques. It is also worth noting that the mechanical constraints imposed on different cell types can shift the requirement for additional components, including the dependency toward the actin cytoskeleton, whose involvement during endocytosis has been shown to increase with membrane tension (Boulant et al., 2011). In agreement with both works, the clathrin–adaptor ratio and membrane tension were shown to regulate the flat-to-curved transition of the clathrin coat during endocytosis (Bucher et al., 2018). Another possibility is that changes in the packing of the tripod as a consequence of the lengthening and rotation of the CHC terminal domain described in our in silico analysis could alter the ability of the uncoating ATPase hsc70 to interact with clathrin, thus reducing uncoating rates (Rapoport et al., 2008). Lastly, additional alternative splicing events occurring in genes encoding endocytosis components could also take place during differentiation and promote the transition between cells producing exclusively canonical coated pits and those forming clathrin plaque.

We also demonstrated that splicing regulation of *CTLC*-ex31 is essential for skeletal muscle development and muscle fiber organization. During muscle development, the structure of clathrin's trimerization domain switched from the embryonic clathrin isoform to the *CLTC*-ex31 muscle isoform in adults. We showed by forced in vivo exon skipping that lack of the *CLTC*-ex31 muscle isoform impairs muscle architecture and force generation. These results indicate that the absence of these seven amino acids directly impacts clathrin function in muscle and produces a defective adhesion phenotype previously observed upon in vivo clathrin depletion (Vassilopoulos et al., 2014). Interestingly, we described an abnormal splicing of *CLTC*-ex31 in skeletal muscle cells and tissue from cDM1 patients. This genetic disease caused by the expression of expanded microsatellite repeats is associated with a spliceopathy due to altered activities of MBNL and CELF splicing factors. Among other splicing defects, we observed a correlation between *CLTC*-ex31 splicing and muscle disease severity in cDM1 patients. Analysis of clathrin ultrastructure and CME activity performed on patient myotubes confirmed their myoblast immature-like phenotype, similar to the experimental *CLTC*-ex31 skipping performed on control myotubes. This observation also raises the question of the involvement of *CLTC*-ex31 misplicing in the immature muscle phenotype described in cDM1 (Farkas-Bargeton et al., 1988). Ultrastructural abnormalities observed in *Cltc* exon 31 skipped fibers, such as detachment of the contractile apparatus and subsarcolemmal disorganizations reminiscent of ringed fibers, have been reported in several muscular dystrophies including DM1 (Brooke and Engel, 1969; Harper, 2001; Schröder and Adams, 1968). However, the presence of detachments between the sarcolemma and underlying sarcomeres was shown to be a characteristic feature of CHC depletion in skeletal muscle (Vassilopoulos et al., 2014), suggesting that this phenotype could be associated with clathrin loss of function and defective plaque formation. Thus, we suggest that abnormal splicing switch of *CLTC* exon 31 could directly contribute to the muscle fiber deterioration observed in severe forms of DM1.

In conclusion, our work identifies *CLTC*-ex31 alternative splicing as a new modulator of clathrin-coated structure plasticity. We reveal how removing or adding a single exon modifies the clathrin polymerization mode and propose that clathrin is genetically regulated to produce functional diversity.

## Materials and methods

### EM

Cultured cells grown on glass coverslips were "unroofed" by sonication as described previously (Heuser, 2000). Platinum replicas of unroofed adherent PMs were then obtained as follows: 2% glutaraldehyde/2% PFA-fixed cells were sequentially treated with 1% OsO4, 1% tannic acid, and 1% uranyl acetate before graded ethanol dehydration and substitution with hexamethyldisilazane (Sigma-Aldrich). Dried samples were then rotary-shadowed with 2 nm of platinum and 5–8 nm of carbon using an ACE600 metal coater (Leica Microsystems). The resultant platinum replica was floated off the glass with hydrofluoric acid (5%), washed several times in distilled water, and picked up on 200-mesh formvar/carbon-coated EM grids. For morphological EM, mouse muscles were fixed by intra-aortic perfusion with 2% PFA and 2% glutaraldehyde in 0.1 M phosphate buffer (pH 7.4). TA samples were postfixed with 2% OsO4 in 0.1 M phosphate buffer (pH 7.4) for 1 h, then dehydrated in a graded series of acetone including a 1% uranyl acetate staining step in 70% acetone, and finally embedded in epoxy resin (EMBed-812; Electron Microscopy Sciences). Ultra-thin (70-nm) sections were then stained with uranyl acetate and lead citrate and mounted on EM grids. Observations of EM grids were made on a Philips CM120 electron microscope operated at 80 kV, and images were recorded with a Morada digital camera (Olympus). Images were processed in Adobe Photoshop to adjust brightness and contrast, and unroofed PMs are presented in inverted contrast.

### Clathrin structure morphometric analysis

Clathrin structures were manually delineated on unroofed PM pictures using ImageJ software (Schneider et al., 2012; National Institutes of Health; https://imagej.nih.gov/ij/) as shown in red in Fig. S3 A. Each object was classified as a CCP or a plaque by the observer; then, the object's area, mean gray value, and minimum

and maximum Feret diameters were measured. Each picture membrane area and the membrane background mean gray value (manually thresholded to exclude clathrin structures) were also measured for normalization and background subtraction purposes. Observer manual classification was used for quantification of size and density (object count normalized by membrane area). Each clathrin structure curvature was calculated as its mean gray value minus the mean membrane background, as shown in Fig. S3 A. Objects were presented on dot plots using the curvature and area parameters and were segregated into four quadrants using an area cutoff threshold of 40,000 $nm^2$, corresponding to the size of the largest CCPs encountered with diameters of ∼200 nm and an empirical curvature threshold set at 35 (out of the 256 gray levels on an 8-bit image, with mean gray background level subtraction) based on manual observer classification of plaques in control membranes. The percentage of objects in each quadrant was reported. A method to further subclassify the objects into eight classes using their ellipticity is presented in Fig. S3. An object's ellipticity was measured as 1 minus the minimum Feret diameter over the maximum Feret diameter. The ellipticity cutoff threshold was placed at 0.33, corresponding to objects having a long axis 1.5 times bigger than their short axis.

### Immunofluorescence and light microscopy

Cells grown on coverslips were washed in warm PBS, fixed 15 min in PFA (4% in PBS) and then washed with cold PBS, permeabilized for 10 min (0.5% Triton X-100 in PBS), and blocked for 30 min (5% BSA in PBS with 0.1% Triton X-100). Primary antibodies were incubated overnight at 4°C in blocking solution (AP2: Abcam; ab2730, Research Resources Identifier [RRID]:AB_303255 at 6 µg/ml, and CHC: Abcam; ab21679, RRID: AB_2083165 at 5 µg/ml) and washed with 0.1% Triton X-100 in PBS; secondary antibodies (Life Technologies; Alexa Fluor 488 and 568) were incubated 1 h in blocking solution and washed, and samples were mounted in Vectashield medium (Vector Laboratories). Imaging was performed on a confocal Nikon Ti2 microscope equipped with a motorized stage and a Yokogawa CSU-W1 spinning disk head coupled with a Prime 95 sCMOS camera (Photometrics) and a 100×/1.43 NA oil-immersion objective at 20°C ambient temperature. Alexa Fluor 488 and Alexa Fluor 568 were sequentially excited using lasers with wavelengths of 488 and 561 nm, respectively. Images were acquired at super resolution using a LiveSR module (Gataca Systems) and Metamorph 7.4 software.

### Cell cultures

Human AB1167 immortalized myoblasts (20-yr-old male, normal fascia lata muscle origin; MyoBank-AFM (Association Française contre les Myopathies) and the platform for immortalization of human cells, Centre of Research in Myology-UMRS974, Paris, France) were grown over 1% Matrigel matrix–coated (Corning; 354230) glass in proliferation medium (DMEM 20% FBS, 50 U/ml penicillin, and 50 mg/ml streptomycin). For DM1 in vitro studies, human primary myoblasts (Arandel et al., 2017; Q12 control cells from the quadriceps muscle of a 12-yr-old child and ASADM11 cells from the gastrocnemius muscle of an 11-yr-old female patient suffering from an infantile DM1 form) were grown over 0.5% gelatin-coated (Sigma-Aldrich; G1890-100G) culture dishes in proliferation medium. Kns4/1 immortalized mouse myoblasts (obtained from the platform for immortalization of human cells, Centre of Research in Myology-UMRS974) were extracted from wild-type C57BL6 mice; FACS sorted to select $Vcam^+$, α7-$integrin^+$, $CD31^-$, $CD45^-$, and $Sca1^-$ cells to exclude contaminant fibroblasts; and grown as described for AB1167 cells. Myoblast immortalization was performed as described by Arandel et al. (2017). AB1167 and Kns4/1 myoblast differentiation into myotubes was induced using 5% horse serum and 10 µg/ml insulin (Sigma-Aldrich; 91077C-1g) in DMEM for 7–12 d depending on the experiment. Q12 and ASADM11 cell differentiation was induced by 4-d serum deprivation and 5 µg/ml insulin supplementation in DMEM medium (50 U/ml penicillin and 50 mg/ml streptomycin). C2C12 cells (ATCC, American Tissue Culture Collection; CRL-1772) were grown in proliferation medium (DMEM 20% FBS, 50 U/ml penicillin, and 50 mg/ml streptomycin), and differentiation was induced by serum deprivation over 4 d. In vitro AAV transduction was achieved by introducing the vector in differentiation medium to reach 40,000 MOI (viral genomes [vg] per cell) on AB1167 myotubes differentiated for 3 d, and RNA extraction, transferrin assay, or unroofing was performed 5 d after transduction. Kns4/1 transduction was done at the same MOI, but the vector was introduced at 5 d of differentiation with experiments performed 7 d after transduction. Rat hippocampal neurons were cultured following the Banker method, above a feeder glia layer (Kaech and Banker, 2006). Briefly, 12- or 18-mm-diameter round #1.5H coverslips were affixed with paraffin dots as spacers, then treated with poly-L-lysine. Hippocampi from E18 rat pups were dissected and homogenized by trypsin treatment followed by mechanical trituration and seeded on the coverslips at a density of 4,000–8,000 cells/$cm^2$ for 3 h in serum containing plating medium. Coverslips were then transferred, cells down, to Petri dishes containing confluent glia cultures conditioned in B27-supplemented neurobasal medium and cultured in these dishes for up to 15 d. Neurons were fixed at 1 or 15 d of in vitro culture. Human iPSCs (C56C2; provided by Dr. Cécile Martinat, I-Stem INSERM/UMR861, Evry, France) were grown in StemMACS iPS-Brew XF (Miltenyi Biotec; 130-107-086).

For RNA interference, transfections were performed using Lipofectamine RNAiMAX reagent (Thermo Fisher Scientific; 13778075) using a 50-nM final concentration of double-stranded antisense RNA against *CELF1* and 2 (passenger strand 5′-GCC AGAAGGAAGGUCCAGA-3′, with two deoxythymidine nucleotide 3′ overhangs) and control siRNA (Eurogentec; SR-CL000-005).

### Transferrin assay

Cells were incubated in DMEM without FBS for 45 min at 37°C. Alexa Fluor 488 fluorescently labeled human transferrin (40 µg/ml; Life Technologies; T13342) was then incubated 15 min on cells, and endocytosis of this compound was stopped with ice-cold PBS washing followed by 4% PFA fixation and final mounting in Vectashield medium. Fluorescence from myoblasts or myotube areas was acquired using a confocal Nikon Ti2 microscope as stack images with 500-nm Z steps using a 40×/1.3 NA oil

objective at 20°C ambient temperature. Each cell fluorescent-positive surface was quantified on a stack projection using ImageJ software by measuring the integrated density (mean gray value) of the background subtracted from that of the cell and normalizing this value to the total cell area.

### Structural model and in silico analysis

CHC trimers were rendered using VMD software (Humphrey et al., 1996) and the 3iyv.pdb structure (Fotin et al., 2004). Secondary structures were 3D modeled as canonical α-helices with backbone torsion angles $\phi = -60°$ and $\psi = -40$ using the 3D Hydrophobic Moment Vector Calculator (3D-HM; Reißer et al., 2014), and surfaces were rendered using University of California, San Francisco Chimera software (RRID:SCR_004097; Pettersen et al., 2004). The hydrophobic moment that is a measure of the helix amphiphilicity (Eisenberg et al., 1982) was calculated along the α-helix over 11 residues with a one-residue increment using HeliQuest (http://heliquest.ipmc.cnrs.fr/; Gautier et al., 2008). Coiled-coil interaction predictions were performed using the nCoils method (Lupas et al., 1991).

### AAV production and titration

The AAV vector plasmid pSMD2 (Snyder et al., 1997) containing a modified mouse U7snRNA gene (Goyenvalle, 2012) was altered using XbaI and StyI restriction sites (surrounding the U7snRNA) and PCR-based fragment assembly using the Gibson method (NEBuilder HiFi DNA master mix; New England Biolabs) in order to replace its antisense sequence with a BsmI restriction enzyme site. The pSMD2-U7-BsmI plasmid obtained enabled further subcloning of the antisense sequences of interest in the U7 exon skipping construct. Specifically, the AAV vector plasmid pSMD2-U7-mCLTCex31 designed to skip exon 31 of both human and mouse *CLTC* mRNA was obtained by subcloning an antisense sequence covering both the splicing acceptor site of exon 30 and the splicing donor site of exon 31 (5′-ACTTTCACCTTTTCC TTTATTGCATCAACCTGCAAAGGAA-3′), fused with a splicing repressor tail (5′-TATGATAGGGACTTAGGGTG-3′), enhancing exon skipping efficiency (Burd and Dreyfuss, 1994). AAV1 viral vectors were prepared by tri-transfection in 293 cells using polyethylenimine transfection agent and the AAV vector plasmid described above (pSMD2-U7-mCLTCex31), the pXX6 plasmid coding for the viral sequences essential for AAV production, and the p0001 plasmid coding for serotype 1 capsid. Vector particles were purified on iodixanol gradient and concentrated on Amicon Ultra-15 100K columns (Merck-Millipore). The AAV-U7-CLTCex31 vector was titrated as vg per milliliter by quantitative real-time PCR using ITR2 (inverted terminal repeats) specific primers at a 60°C annealing temperature (forward 5′-CTCCATCACTAGGGG TTCCTTG-3′ and reverse 5′-GTAGATAAGTAGCATGGC-3′) and the MGB Taqman probe 5′-TAGTTAATGATTAACCC-3′.

### In vivo experiments

8-wk-old female FVB mice (FVB/NRj; Janvier; Cat #SC-FVBN-F) were anesthetized by isoflurane for AAV-U7-CLTCex31 i.m. administration of two 45-µl injections of vector over a period of 24 h using a 30-G needle in the left TA muscle. The right contralateral TA muscle was injected with the same volume of PBS as control. A dose–response study was performed with i.m. injections of vector doses ranging from 0.82 to $3.52 \times 10^{11}$ vg (1–2 mice per group), and the optimal AAV-U7-CLTCex31 exon skipping dose was defined as $1.44 \times 10^{11}$ vg. For muscle function assessment, the mice were injected at this optimal dose, and then sacrificed 1 or 2 mo post injection (PI; $n = 6$ and $n = 7$ mice per group at 1 and 2 mo PI, respectively). At the end of the procedure, either mice were sacrificed to collect TA muscles (dose–response study 1 mo PI) or muscle function was analyzed before sacrifice and TA collection (optimal AAV dose and saline contralateral injections; $n = 5$–7 mice; see figure legends for details). Mice were killed by cervical dislocation, and both AAV- and control-injected TA muscles were frozen in liquid nitrogen–cooled isopentane, and cryosections were performed for histological analysis and RNA extraction. Conventional hematoxylin and eosin histochemical staining was performed on 8-µm TA transversal cryosections with final mounting using Eukitt (Sigma-Aldrich), and images were acquired on an Axio Lab.A1 light microscope (Zeiss) at 20°C ambient temperature using a ToupTek 5.1 MP CMOS camera, a 20×/0.45 NA objective, and Toupview software (ToupTek). All mice used in this study were housed on a 12-h light/dark cycle and received standard diet and water ad libitum in the animal facility of the Sorbonne University, Paris.

### Study approval

Mice studies conformed to French laws and regulations concerning the use of animals for research and were approved by an external ethics committee (approval no. 13333-2018013111391590 v2 delivered by the French Ministry of Higher Education and Scientific Research). The use of Wistar rats followed the guidelines established by the European Animal Care and Use Committee (86/609/CEE) and was approved by the local ethics committee (agreement D13-055-8).

### Muscle contractile properties

The isometric contractile properties of TA muscles were studied in situ on mice anesthetized with 60 mg/kg pentobarbital. The distal tendon of the muscle was attached to the lever arm of a servomotor system (305B Dual-Mode Lever; Aurora Scientific). The sciatic nerve was stimulated by a bipolar silver electrode using a supramaximal (10 V) square wave pulse. The optimal length (L0) at which the muscle developed its maximal isometric strength was defined using several 100-ms tetanic stimulations of 75 Hz. After a 60-s recovery time, myograms were recorded at L0 in response to a 500-ms electrical stimulation at 100-Hz frequency, and the absolute maximal isometric tetanic force and relaxation phase were measured. Another 60-s pause later, eccentric contractions were performed to measure P1 to P10 maximal tetanic force while stretching the muscle by an extra 10% of L0 with 10 successive 150-Hz stimulations spaced by 45 s. Mice were sacrificed by cervical dislocation, and TA muscles were weighted and then frozen for histology as described above. Peak isometric force (P0) was normalized by muscle mass and expressed in Newton per milligram. Specific maximal eccentric forces (P1 to P10) were normalized by muscle mass and presented as the percent variation between AAV-treated muscle and contralateral muscle.

### RNA extraction and RT-PCR

Total RNA was isolated using TRIZOL reagent (Life Technologies; 15596018) from TA muscle or cell cultures. Control human

fetal muscle RNA samples were described in Rau et al. (2015), and cDM1 and SMA control RNA were from bicep muscle biopsies of 3–61-wk-old infants described by Nakamori et al. (2017). RNA from iPSCs differentiated into myotubes was kindly given by Dr. Cécile Martinat. Total RNA (1 µg) was submitted to reverse transcription using murine leukemia virus reverse transcription and oligo $dT_{12–18}$ (Life Technologies). PCR was performed using 25 ng cDNA diluted in Platinum Taq polymerase mix containing 1.5 mM $MgCl_2$ (Invitrogen) and 0.2 µM primers in a final volume of 25 µl. Cycling conditions consisted of a polymerase activation step at 94°C for 5 min followed by 35 cycles of three steps: 30 s of denaturation at 94°C, 30 s of annealing at appropriate temperature, and 25 s of extension at 72°C. For human *CLTC*-ex31 PCR as well as for vervet monkey (BS-C-1 cells), forward primer 5′-TGCCCTATTTCATCCAGGTCA-3′ and reverse primer 5′-ATGGGTTGTGTCTCTGTAGC-3′ were annealed at 57°C. For mouse and rat *Cltc*-ex31 PCR, forward primer 5′-GAAACCGCATGGAGACATAA-3′ and reverse primer 5′-AAACAATGGGCTGTGTCTCTG-3′ were annealed at 56°C. Gel electrophoresis of PCR products was performed in 2.5% agarose, and images were acquired on a Geni2 gel imaging system (Ozyme). The densitometric analysis of PCR bands was realized using ImageJ software, and the PSI value corresponding to the fraction of mRNAs that contained an exon was calculated as the ratio of the density of the exon inclusion band to the sum of the densities of inclusion and exclusion bands, expressed as a percentage.

### Western blot and immunoprecipitation

Cell cultures were lysed in a buffer (50 mM Tris-HCl, pH 7.5, 0.15 M NaCl, 1 mM EDTA, and 1% NP-40) supplemented with protein inhibitor cocktail 1:100 (Sigma-Aldrich). Samples denatured by 3 min of boiling in Laemmli buffer were separated by electrophoresis on 4–12% bis-acrylamide gel (Life Technologies), transferred to 0.45-µm nitrocellulose membranes (Life Technologies), and labeled with primary antibodies (AP2: Abcam; ab2807; RRID:AB_2056323 at 4 µg/ml; CHC: Abcam; ab21679; RRID:AB_2083165 at 1 µg/ml; CLCa: Proteintech; 10852-1-AP; RRID:AB_2083025 at 0.8 µg/ml; GAPDH: Santa Cruz; sc-25778; RRID:AB_10167668 at 0.05 µg/ml; and PICALM: Abcam; ab106409; RRID:AB_10863339 at 2 µg/ml) and then a secondary antibody coupled to HRP (Trueblot IgG HRP; Rockland). The presence of proteins in samples was detected using Immobilon Western Chemiluminescent HRP Substrate (Sigma-Aldrich), and image acquisition was performed on a G-Box (Ozyme). Western blot quantification (Fig. S2 A) was performed using ImageLab software 6.0.1 (Bio-Rad) by normalizing AP2 signal by corresponding GAPDH signal and calculating fold-change relative to the myoblast stage. For CHC immunoprecipitation, myotube lysates of 450 µg protein content were prepared in lysis buffer, precleared twice with 30 µl Protein G Sepharose (PGS; 4 fast flow; Thermo Fisher Scientific); and incubated with 5 µg of CHC antibody overnight (4°C). Washed PGS (40 µl) was incubated with sample lysates for 2 h at 4°C. Pelleted PGS was then denatured by 3 min of boiling in Laemmli buffer and subjected to electrophoresis and immunoblotting as described above.

### Proteomics and mass spectrometry (MS) analysis

Human myoblasts and myotubes differentiated for 4 d were lysed in a buffer (50 mM Tris-HCl, pH 7.5, 0.15 M NaCl, 1 mM EDTA, and 1% NP-40) supplemented with protein inhibitor cocktail 1:100. CHC immunoprecipitation was then performed on 300 µg protein lysates prepared in lysis buffer, precleared with 30 µl PGS, and incubated with 5 µg CHC antibody (Abcam; ab21679; RRID:AB_2083165) overnight at 4°C. Washed PGS (30 µl) was incubated with sample lysates for 2 h at 4°C. Pelleted PGS was then washed once with lysis buffer lowered to 0.1% NP-40, then thrice with ammonium bicarbonate $(NH_4)HCO_3$ 25 mM before on-beads digestion with endoproteinase Glu-C. Five biological replicates of myoblasts or myotubes were on-beads digested (15 µl beads) with 0.5 µg of Glu-C (Promega; V1651) for 1 h in 100 µl of 25 mM $(NH_4)HCO_3$. Samples were then loaded onto homemade C18 StageTips for desalting. Peptides were eluted using 40/60 methyl cyanide/$H_2O$ + 0.1% formic acid, vacuum concentrated to dryness, and reconstituted in injection buffer (2% methyl cyanide/0.3% trifluoroacetic acid) before nano–liquid chromatography (LC)–tandem MS analysis. LC was performed with an RSLCnano system (Ultimate 3000; Thermo Fisher Scientific) coupled online to a Q Exactive HF-X mass spectrometer with a Nanospay Flex ion source (Thermo Fisher Scientific).

For quantification, Glu-C peptides were first trapped on a C18 column (75-µm inner diameter × 2 cm; nanoViper Acclaim PepMapTM 100; Thermo Fisher Scientific) with buffer A (2/98 MeCN/$H_2O$ in 0.1% formic acid) at a flow rate of 2.5 µl/min over 4 min. Separation was then performed on a 50-cm × 75-µm C18 column (nanoViper Acclaim PepMapTM RSLC, 2 µm, 100 Å; Thermo Fisher Scientific) regulated to a temperature of 50°C with a linear gradient of 2% to 30% buffer B (100% MeCN in 0.1% formic acid) at a flow rate of 300 nL/min over 91 min. MS full scans were performed in the ultra-high–field Orbitrap mass analyzer in the range of 375–1,500 m/z with a resolution of 120,000 at 200 m/z. The top 20 intense ions were subjected to Orbitrap for further fragmentation via high-energy collision dissociation activation and a resolution of 15,000 with the intensity threshold kept at $1.3 \times 10^5$. We selected ions with a charge state from 2+ to 6+ for screening. Normalized collision energy was set at 27 and a dynamic exclusion of 40 s.

For identification, the data were searched against the *Homo sapiens* (UP000005640) UniProt database and the CHC Q00610 ± ex31 sequences using Sequest Proteome Discoverer (version 2.4; RRID:SCR_014477). Enzyme specificity was set to Glu-C, and a maximum of two missed cleavage sites was allowed. Oxidized methionine, Met-loss, Met-loss-Acetyl, and N-terminal acetylation were set as variable modifications. Maximum allowed mass deviation was set to 10 ppm for monoisotopic precursor ions and 0.02 D for MS/MS peaks. The resulting files were further processed using myProMS v3.9 (Poullet et al., 2007). False discovery rate calculation was performed using Percolator (RRID:SCR_005040) and was set to 1% at the peptide level for the whole study. To quantify the specific peptides of CHC with ± exon 31, corresponding to peptides YLTKVDAIKE (+exon 31 393.892 m/z; charged 3+) and YLTKVDKLDASE (−exon 31 691.364 m/z; charged 2+), we extracted from the MS survey of the nanoLC-MS/MS raw files the extracted ion chromatogram (XIC) signal using the retention time and m/z values of the well-characterized Glu-C peptide ions using Xcalibur software (manually; RRID:SCR_014593). Specific peptide XIC areas were integrated in Xcalibur under the QualBrowser

interface using the ICIS algorithm, and the sum of all clathrin peptide XIC areas were computed for each biological replicate with MassChroQ version 2.2 (Valot et al., 2011) for normalization.

The MS proteomics data have been deposited in the ProteomeXchange Consortium via the PRIDE (Perez-Riverol et al., 2019) partner repository, with the dataset identifier PXD018333.

### Statistics

Histograms express the means ± SEM unless otherwise stated in the figure legends. Transferrin assay box plots show medians extended from the 25th to the 75th percentiles, minimum and maximum data point whiskers, and mean as a cross. Differences between two groups were tested by using the nonparametric Mann-Whitney test when data did not have a Gaussian distribution assessed by a normality test. Unpaired Mann-Whitney tests with two-tailed P value were performed for transferrin assays and morphometric analysis. A paired *t* test was performed for muscle mass comparison, since each animal was its own control, with the injection of both TA muscles with either the AAV vector or saline, and the test was set in a bilateral fashion as no assumption was made regarding the putative orientation of muscle mass variation. Finally, differences between AAV-treated and saline contralateral muscle groups were tested using the Wilcoxon matched-pairs test with one-tailed P value. Since our experimental hypothesis is the phenocopy of an immature muscle, we therefore tested for functional degradation in one direction only (either a force decrease or a relaxation time increase). Statistical significance was defined by a P value <0.05 for all experiments, and the following legend was used in all figures: *, $P \le 0.05$; **, $P \le 0.005$; ***, $P \le 0.0001$; and n.s., nonsignificant.

### Online supplemental material

Fig. S1 presents supporting data on *CLTC* exon 31 alternative splicing in various cell types. Fig. S2 presents supporting protein expression and transcriptomic and proteomic data on CHC exon 31 alternative splicing in human muscle cells. Fig. S3 shows morphometric analysis of clathrin-coated structures on PREM images. Fig. S4 shows *Cltc*-ex31 in vitro skipping in murine myotubes. Fig. S5 shows in vivo exon skipping protocol validation and supplementary histological and functional data.

## Acknowledgments

We thank the MYOVECTOR technical platform of the Centre of Research in Myology-UMRS974 (Paris, France) for AAV production, the Institut de Biologie Paris Seine Electron Microscopy platform (Sorbonne University, Paris, France), and the Penn Vector Core, Gene Therapy Program, (University of Pennsylvania, Philadelphia, PA) for providing the pAAV1 plasmid (p0001); and the MyoBank-AFM and the platform for immortalization of human cells from the Institut de Myologie (Paris, France). We also thank Cécile Martinat, Alain Sureau (Centre de Recherche en Myologie, UMRS 974, Paris, France), and Lorenzo Giordano (Centre de Recherche en Myologie, UMRS 974) for materials/reagents, Frédérique Rau and Ozgur Ogut for comments, and Vanessa Masson for her technical assistance during the MS study.

This work was funded by Sorbonne Université, Institut National de la Santé et de la Recherche Médicale, Association Institut de Myologie, the Agence Nationale de la Recherche (grants ANR-14-CE12-0001-01 to S. Vassilopoulos, ANR-14-CE12-0009 to M. Bitoun, and ANR-16-CE17-0018 to D. Furling), Tokyo National Center of Neurology and Psychiatry (funding 29-4 to M. Nakamori), and Région Ile-de-France and Fondation pour la Recherche Médicale grants (to D. Loew).

The authors declare no competing financial interests.

Author contributions: G. Moulay: conceptualization, formal analysis, investigation, methodology, visualization, writing—original draft, review, and editing. J. Lainé, M. Lemaître, M. Nakamori, I. Nishino, G. Caillol, F. Dingli, D. Loew, and C. Leterrier: formal analysis, investigation, review, and editing. K. Mamchaoui and L. Julien: methodology and resources. M. Bitoun and D. Furling: conceptualization, formal analysis, funding acquisition, investigation, methodology, supervision, writing, review, and editing. S. Vassilopoulos: conceptualization, formal analysis, funding acquisition, investigation, methodology, visualization, supervision, writing—original draft, review, and editing.

Submitted: 11 December 2019
Revised: 14 April 2020
Accepted: 15 May 2020

## References

Arandel, L., M. Polay Espinoza, M. Matloka, A. Bazinet, D. De Dea Diniz, N. Naouar, F. Rau, A. Jollet, F. Edom-Vovard, K. Mamchaoui, et al. 2017. Immortalized human myotonic dystrophy muscle cell lines to assess therapeutic compounds. *Dis. Model. Mech.* 10:487–497. https://doi.org/10.1242/dmm.027367

Avinoam, O., M. Schorb, C.J. Beese, J.A.G. Briggs, and M. Kaksonen. 2015. ENDOCYTOSIS. Endocytic sites mature by continuous bending and remodeling of the clathrin coat. *Science*. 348:1369–1372. https://doi.org/10.1126/science.aaa9555

Blue, R.E., A. Koushik, N.M. Engels, H.J. Wiedner, T.A. Cooper, and J. Giudice. 2018. Modulation of alternative splicing of trafficking genes by genome editing reveals functional consequences in muscle biology. *Int. J. Biochem. Cell Biol.* 105:134–143. https://doi.org/10.1016/j.biocel.2018.10.004

Boucrot, E., S. Saffarian, R. Zhang, and T. Kirchhausen. 2010. Roles of AP-2 in clathrin-mediated endocytosis. *PLoS One*. 5. e10597. https://doi.org/10.1371/journal.pone.0010597

Boulant, S., C. Kural, J.-C. Zeeh, F. Ubelmann, and T. Kirchhausen. 2011. Actin dynamics counteract membrane tension during clathrin-mediated endocytosis. *Nat. Cell Biol.* 13:1124–1131. https://doi.org/10.1038/ncb2307

Brodsky, F.M.. 2012. Diversity of clathrin function: new tricks for an old protein. *Annu. Rev. Cell Dev. Biol.* 28:309–336. https://doi.org/10.1146/annurev-cellbio-101011-155716

Brooke, M.H., and W.K. Engel. 1969. The histographic analysis of human muscle biopsies with regard to fiber types. 3. Myotonias, myasthenia gravis, and hypokalemic periodic paralysis. *Neurology*. 19:469–477. https://doi.org/10.1212/WNL.19.5.469

Bucher, D., F. Frey, K.A. Sochacki, S. Kummer, J.-P. Bergeest, W.J. Godinez, H.-G. Kräusslich, K. Rohr, J.W. Taraska, U.S. Schwarz, et al. 2018. Clathrin-adaptor ratio and membrane tension regulate the flat-to-curved transition of the clathrin coat during endocytosis. *Nat. Commun.* 9:1109. https://doi.org/10.1038/s41467-018-03533-0

Burd, C.G., and G. Dreyfuss. 1994. RNA binding specificity of hnRNP A1: significance of hnRNP A1 high-affinity binding sites in pre-mRNA splicing. *EMBO J.* 13:1197–1204. https://doi.org/10.1002/j.1460-2075.1994.tb06369.x

Chetrit, D., N. Ziv, and M. Ehrlich. 2009. Dab2 regulates clathrin assembly and cell spreading. *Biochem. J.* 418:701–715. https://doi.org/10.1042/BJ20081288

Dambournet, D., K.A. Sochacki, A.T. Cheng, M. Akamatsu, J.W. Taraska, D. Hockemeyer, and D.G. Drubin. 2018. Genome-edited human stem cells expressing fluorescently labeled endocytic markers allow quantitative analysis of clathrin-mediated endocytosis during differentiation. *J. Cell Biol.* 217:3301–3311. https://doi.org/10.1083/jcb.201710084

De Deyne, P.G., A. O'Neill, W.G. Resneck, G.M. Dmytrenko, D.W. Pumplin, and R.J. Bloch. 1998. The vitronectin receptor associates with clathrin-coated membrane domains via the cytoplasmic domain of its beta5 subunit. *J. Cell Sci.* 111:2729–2740.

den Otter, W.K., and W.J. Briels. 2011. The generation of curved clathrin coats from flat plaques. *Traffic.* 12:1407–1416. https://doi.org/10.1111/j.1600-0854.2011.01241.x

Dillman, A.A., D.N. Hauser, J.R. Gibbs, M.A. Nalls, M.K. McCoy, I.N. Rudenko, D. Galter, and M.R. Cookson. 2013. mRNA expression, splicing and editing in the embryonic and adult mouse cerebral cortex. *Nat. Neurosci.* 16:499–506. https://doi.org/10.1038/nn.3332

Eisenberg, D., R.M. Weiss, and T.C. Terwilliger. 1982. The helical hydrophobic moment: a measure of the amphiphilicity of a helix. *Nature.* 299:371–374. https://doi.org/10.1038/299371a0

Farkas-Bargeton, E., J.P. Barbet, S. Dancea, R. Wehrle, A. Checouri, and O. Dulac. 1988. Immaturity of muscle fibers in the congenital form of myotonic dystrophy: its consequences and its origin. *J. Neurol. Sci.* 83:145–159. https://doi.org/10.1016/0022-510X(88)90064-0

Fotin, A., Y. Cheng, P. Sliz, N. Grigorieff, S.C. Harrison, T. Kirchhausen, and T. Walz. 2004. Molecular model for a complete clathrin lattice from electron cryomicroscopy. *Nature.* 432:573–579. https://doi.org/10.1038/nature03079

Franck, A., J. Lainé, G. Moulay, E. Lemerle, M. Trichet, C. Gentil, S. Benkhelifa-Ziyyat, E. Lacène, M.T. Bui, G. Brochier, et al. 2019. Clathrin plaques and associated actin anchor intermediate filaments in skeletal muscle. *Mol. Biol. Cell.* 30:579–590. https://doi.org/10.1091/mbc.E18-11-0718

Fugier, C., A.F. Klein, C. Hammer, S. Vassilopoulos, Y. Ivarsson, A. Toussaint, V. Tosch, A. Vignaud, A. Ferry, N. Messaddeq, et al. 2011. Misregulated alternative splicing of BIN1 is associated with T tubule alterations and muscle weakness in myotonic dystrophy. *Nat. Med.* 17:720–725. https://doi.org/10.1038/nm.2374

Gautier, R., D. Douguet, B. Antonny, and G. Drin. 2008. HELIQUEST: a web server to screen sequences with specific α-helical properties. *Bioinformatics.* 24:2101–2102. https://doi.org/10.1093/bioinformatics/btn392

Giudice, J., Z. Xia, E.T. Wang, M.A. Scavuzzo, A.J. Ward, A. Kalsotra, W. Wang, X.H.T. Wehrens, C.B. Burge, W. Li, et al. 2014. Alternative splicing regulates vesicular trafficking genes in cardiomyocytes during postnatal heart development. *Nat. Commun.* 5:3603. https://doi.org/10.1038/ncomms4603

Giudice, J., J.A. Loehr, G.G. Rodney, and T.A. Cooper. 2016. Alternative Splicing of Four Trafficking Genes Regulates Myofiber Structure and Skeletal Muscle Physiology. *Cell Rep.* 17:1923–1933. https://doi.org/10.1016/j.celrep.2016.10.072

Goyenvalle, A.. 2012. Engineering U7snRNA gene to reframe transcripts. *Methods Mol. Biol.* 867:259–271. https://doi.org/10.1007/978-1-61779-767-5_17

Grove, J., D.J. Metcalf, A.E. Knight, S.T. Wavre-Shapton, T. Sun, E.D. Protonotarios, L.D. Griffin, J. Lippincott-Schwartz, and M. Marsh. 2014. Flat clathrin lattices: stable features of the plasma membrane. *Mol. Biol. Cell.* 25:3581–3594. https://doi.org/10.1091/mbc.e14-06-1154

Harper, P.S. 2001. Myotonic Dystrophy. Third edition. W.B. Saunders, London, UK. 436 pp.

Heuser, J.. 1980. Three-dimensional visualization of coated vesicle formation in fibroblasts. *J. Cell Biol.* 84:560–583. https://doi.org/10.1083/jcb.84.3.560

Heuser, J.. 2000. The production of 'cell cortices' for light and electron microscopy. *Traffic.* 1:545–552. https://doi.org/10.1034/j.1600-0854.2000.010704.x

Humphrey, W, A Dalke, and K Schulten. 1996. VMD: visual molecular dynamics. *J Mol Graph.* 14:33–38. https://doi.org/10.1016/0263-7855(96)00018-5

Jones, D.T.. 1999. Protein secondary structure prediction based on position-specific scoring matrices. *J. Mol. Biol.* 292:195–202. https://doi.org/10.1006/jmbi.1999.3091

Kaech, S., and G. Banker. 2006. Culturing hippocampal neurons. *Nat. Protoc.* 1:2406–2415. https://doi.org/10.1038/nprot.2006.356

Kanaseki, T., and K. Kadota. 1969. The "vesicle in a basket". A morphological study of the coated vesicle isolated from the nerve endings of the guinea pig brain, with special reference to the mechanism of membrane movements. *J. Cell Biol.* 42:202–220. https://doi.org/10.1083/jcb.42.1.202

Kirchhausen, T.. 2009. Imaging endocytic clathrin structures in living cells. *Trends Cell Biol.* 19:596–605. https://doi.org/10.1016/j.tcb.2009.09.002

Kirchhausen, T., S.C. Harrison, and J. Heuser. 1986. Configuration of clathrin trimers: evidence from electron microscopy. *J. Ultrastruct. Mol. Struct. Res.* 94:199–208. https://doi.org/10.1016/0889-1605(86)90067-4

Lampe, M., S. Vassilopoulos, and C. Merrifield. 2016. Clathrin coated pits, plaques and adhesion. *J. Struct. Biol.* 196:48–56. https://doi.org/10.1016/j.jsb.2016.07.009

Lupas, A., M. Van Dyke, and J. Stock. 1991. Predicting coiled coils from protein sequences. *Science.* 252:1162–1164. https://doi.org/10.1126/science.2520.5009.1162

McMahon, H.T., and E. Boucrot. 2011. Molecular mechanism and physiological functions of clathrin-mediated endocytosis. *Nat. Rev. Mol. Cell Biol.* 12:517–533. https://doi.org/10.1038/nrm3151

Merkin, J., C. Russell, P. Chen, and C.B. Burge. 2012. Evolutionary dynamics of gene and isoform regulation in Mammalian tissues. *Science.* 338:1593–1599. https://doi.org/10.1126/science.1228186

Mettlen, M., D. Loerke, D. Yarar, G. Danuser, and S.L. Schmid. 2010. Cargo- and adaptor-specific mechanisms regulate clathrin-mediated endocytosis. *J. Cell Biol.* 188:919–933. https://doi.org/10.1083/jcb.200908078

Meyerholz, A., L. Hinrichsen, S. Groos, P.-C. Esk, G. Brandes, and E.J. Ungewickell. 2005. Effect of clathrin assembly lymphoid myeloid leukemia protein depletion on clathrin coat formation. *Traffic.* 6:1225–1234. https://doi.org/10.1111/j.1600-0854.2005.00355.x

Nakamori, M., K. Hamanaka, J.D. Thomas, E.T. Wang, Y.K. Hayashi, M.P. Takahashi, M.S. Swanson, I. Nishino, and H. Mochizuki. 2017. Aberrant Myokine Signaling in Congenital Myotonic Dystrophy. *Cell Rep.* 21:1240–1252. https://doi.org/10.1016/j.celrep.2017.10.018

Näthke, I.S., J. Heuser, A. Lupas, J. Stock, C.W. Turck, and F.M. Brodsky. 1992. Folding and trimerization of clathrin subunits at the triskelion hub. *Cell.* 68:899–910. https://doi.org/10.1016/0092-8674(92)90033-9

Perez-Riverol, Y., A. Csordas, J. Bai, M. Bernal-Llinares, S. Hewapathirana, D.J. Kundu, A. Inuganti, J. Griss, G. Mayer, M. Eisenacher, et al. 2019. The PRIDE database and related tools and resources in 2019: improving support for quantification data. *Nucleic Acids Res.* 47(D1):D442–D450. https://doi.org/10.1093/nar/gky1106

Pettersen, E.F., T.D. Goddard, C.C. Huang, G.S. Couch, D.M. Greenblatt, E.C. Meng, and T.E. Ferrin. 2004. UCSF Chimera--a visualization system for exploratory research and analysis. *J. Comput. Chem.* 25:1605–1612. https://doi.org/10.1002/jcc.20084

Poullet, P., S. Carpentier, and E. Barillot. 2007. myProMS, a web server for management and validation of mass spectrometry-based proteomic data. *Proteomics.* 7:2553–2556. https://doi.org/10.1002/pmic.200600784

Rapoport, I., W. Boll, A. Yu, T. Böcking, and T. Kirchhausen. 2008. A motif in the clathrin heavy chain required for the Hsc70/auxilin uncoating reaction. *Mol. Biol. Cell.* 19:405–413. https://doi.org/10.1091/mbc.e07-09-0870

Rau, F., J. Lainé, L. Ramanoudjame, A. Ferry, L. Arandel, O. Delalande, A. Jollet, F. Dingli, K.-Y. Lee, C. Peccate, et al. 2015. Abnormal splicing switch of DMD's penultimate exon compromises muscle fibre maintenance in myotonic dystrophy. *Nat. Commun.* 6:7205. https://doi.org/10.1038/ncomms8205

Reißer, S., E. Strandberg, T. Steinbrecher, and A.S. Ulrich. 2014. 3D hydrophobic moment vectors as a tool to characterize the surface polarity of amphiphilic peptides. *Biophys. J.* 106:2385–2394. https://doi.org/10.1016/j.bpj.2014.04.020

Robinson, M.S.. 2004. Adaptable adaptors for coated vesicles. *Trends Cell Biol.* 14:167–174. https://doi.org/10.1016/j.tcb.2004.02.002

Royle, S.J., and L. Lagnado. 2010. Clathrin-mediated endocytosis at the synaptic terminal: bridging the gap between physiology and molecules. *Traffic.* 11:1489–1497. https://doi.org/10.1111/j.1600-0854.2010.01104.x

Saheki, Y., and P. De Camilli. 2012. Synaptic vesicle endocytosis. *Cold Spring Harb. Perspect. Biol.* 4. a005645. https://doi.org/10.1101/cshperspect.a005645

Schneider, C.A., W.S. Rasband, and K.W. Eliceiri. 2012. NIH Image to ImageJ: 25 years of image analysis. *Nat. Methods.* 9:671–675. https://doi.org/10.1038/nmeth.2089

Schröder, J.M., and R.D. Adams. 1968. The ultrastructural morphology of the muscle fiber in myotonic dystrophy. *Acta Neuropathol.* 10:218–241. https://doi.org/10.1007/BF00687725

Snyder, R.O., S.K. Spratt, C. Lagarde, D. Bohl, B. Kaspar, B. Sloan, L.K. Cohen, and O. Danos. 1997. Efficient and stable adeno-associated virus-mediated transduction in the skeletal muscle of adult immunocompetent mice. *Hum. Gene Ther.* 8:1891–1900. https://doi.org/10.1089/hum.1997.8.16-1891

Sochacki, K.A., and J.W. Taraska. 2019. From Flat to Curved Clathrin: Controlling a Plastic Ratchet. *Trends Cell Biol.* 29:241–256. https://doi.org/10.1016/j.tcb.2018.12.002

Sznajder, Ł.J., and M.S. Swanson. 2019. Short Tandem Repeat Expansions and RNA-Mediated Pathogenesis in Myotonic Dystrophy. *Int. J. Mol. Sci.* 20:3365. https://doi.org/10.3390/ijms20133365

Trapnell, C., D. Cacchiarelli, J. Grimsby, P. Pokharel, S. Li, M. Morse, N.J. Lennon, K.J. Livak, T.S. Mikkelsen, and J.L. Rinn. 2014. The dynamics and regulators of cell fate decisions are revealed by pseudotemporal ordering of single cells. *Nat. Biotechnol.* 32:381–386. https://doi.org/10.1038/nbt.2859

Valot, B., O. Langella, E. Nano, and M. Zivy. 2011. MassChroQ: a versatile tool for mass spectrometry quantification. *Proteomics*. 11:3572–3577. https://doi.org/10.1002/pmic.201100120

Vassilopoulos, S., C. Gentil, J. Lainé, P.-O. Buclez, A. Franck, A. Ferry, G. Précigout, R. Roth, J.E. Heuser, F.M. Brodsky, et al. 2014. Actin scaffolding by clathrin heavy chain is required for skeletal muscle sarcomere organization. *J. Cell Biol.* 205:377–393. https://doi.org/10.1083/jcb.201309096

Wilbur, J.D., P.K. Hwang, J.A. Ybe, M. Lane, B.D. Sellers, M.P. Jacobson, R.J. Fletterick, and F.M. Brodsky. 2010. Conformation switching of clathrin light chain regulates clathrin lattice assembly. *Dev. Cell.* 18:841–848. https://doi.org/10.1016/j.devcel.2010.04.007

Ybe, J.A., S.N. Fontaine, T. Stone, J. Nix, X. Lin, and S. Mishra. 2013. Nuclear localization of clathrin involves a labile helix outside the trimerization domain. *FEBS Lett.* 587:142–149. https://doi.org/10.1016/j.febslet.2012.11.005

# Supplemental material


https://doi.org/10.1083/jcb.201912061

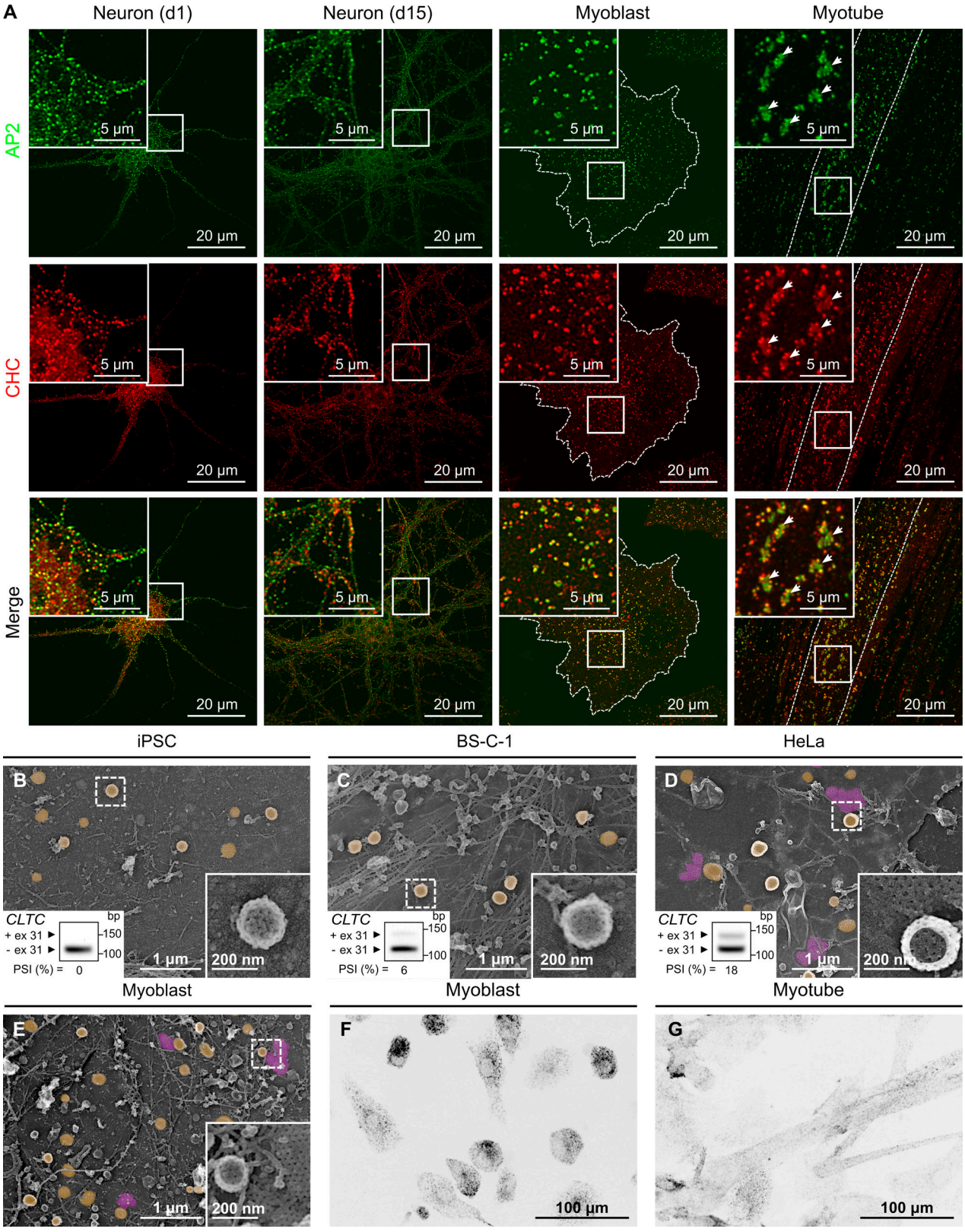


Figure S1. **Supporting data on *CLTC* exon 31 alternative splicing in various cell types.** Related to Fig. 1. **(A)** Separate channels from the super-resolution images presented in Fig. 1 A. Arrows show clathrin plaques. **(B–E)** High-magnification transmission EM views of various unroofed cell types. CCPs are shown in yellow, and plaques are shown in purple, with native grayscale kept in magnification insets. Corresponding RT-PCR electrophoresis of *CLTC* exon 31 alternative splicing is shown at the bottom left. **(B)** Human iPSCs. **(C)** BS-C-1 cells. **(D)** HeLa cells. **(E)** Human myoblasts. All images and insets outlined with dashed rectangles are presented at the same scale for comparison. **(F and G)** Representative images corresponding to myoblast and myotube transferrin uptake assays quantified in Fig. 1 H.

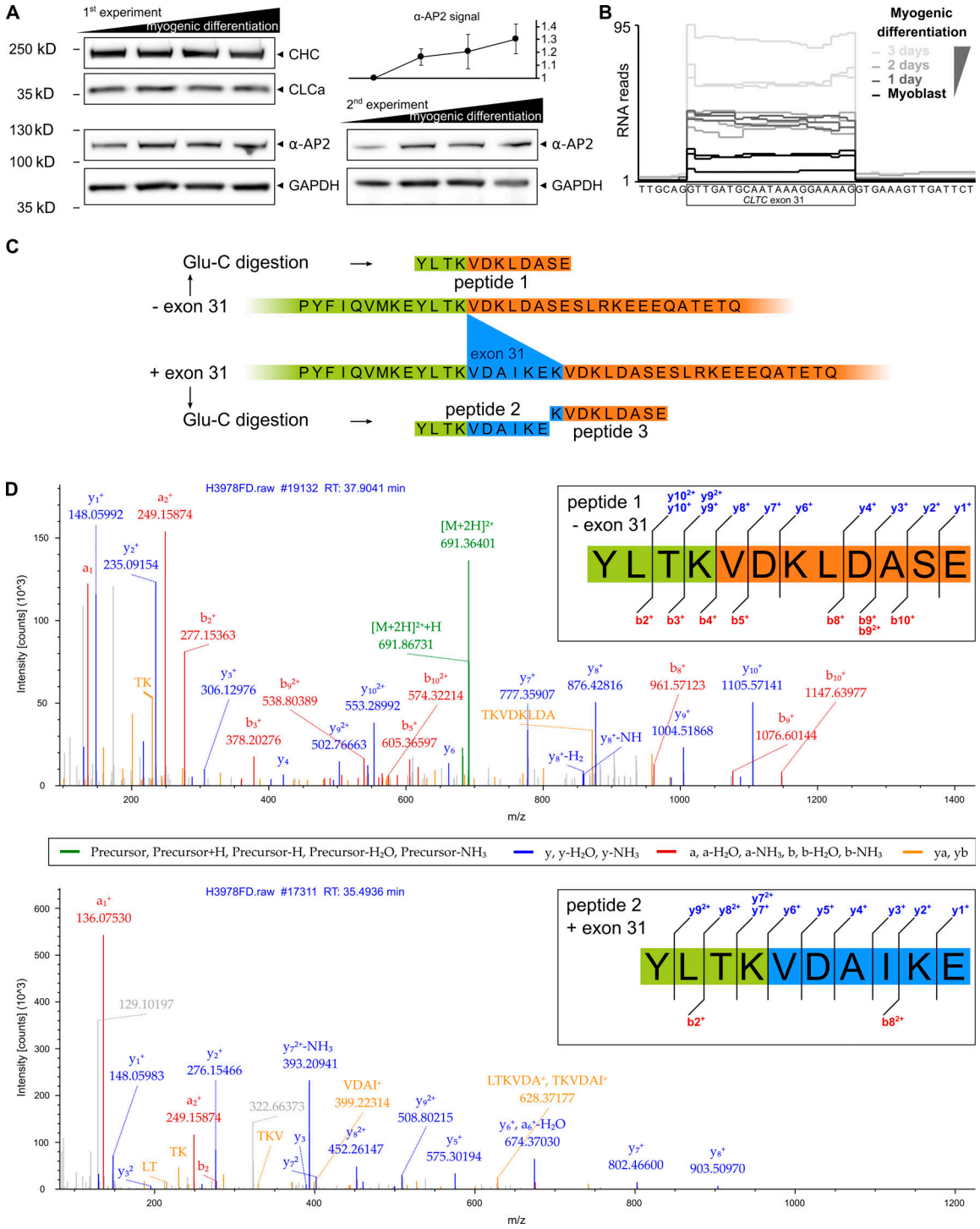


Figure S2. **Supporting protein expression and transcriptomic and proteomic data on CHC exon 31 alternative splicing in human muscle cells.** Related to Fig. 1. **(A)** Immunoblot analysis of cell extracts from human myoblasts (lane 1), and 2, 4, and 7 d differentiated myotubes in lanes 2 to 4 (experiment corresponding to RT-PCR shown in Fig. 1 I). α-AP2: adaptor protein 2 subunit α. A second biological replicate experiment was performed to confirm α-AP2 protein increase during differentiation. The average α-AP2 signal quantified in both experiments is normalized to GAPDH and presented relative to the myoblast stage (error bars correspond to SD). **(B)** Graph of *CLTC* exon 31 region extracted from publicly available transcriptome data (Trapnell et al., 2014) from an in vitro human myogenic differentiation experiment ($n$ = 3 per condition). Raw RNA read density was aligned over the human genome using the WashU Epigenome Browser (dmseq.org). **(C)** Amino acid sequence of human CHC protein in the vicinity of exon 31 (in blue), with exon 30 and exon 32 borders shown in green and orange, respectively. CHC was digested by Glu-C to perform shotgun proteomic analysis, as it is predicted to generate three unique peptides covering the exon junctions and therefore discriminates CHC isoforms arising from exon 31 splicing. Peptide 1 and 2 quantifications are shown in Fig. 1 I; peptide 3 was not quantified due to hydrophilic properties preventing correct retention on the LC column (only detected in two myotube samples out of five). **(D)** Representative MS/MS spectra (search performed with PD 2.4) identifying peptides YLTKVDAIKE (+ex31, 393.892 m/z = $[M+H]^{3+}$) and YLTKVDKLDASE (−ex31, 691.364 m/z = $[M+H]^{2+}$), derived from a Glu-C digestion of the *H. sapiens* CHC protein containing the ±ex31.

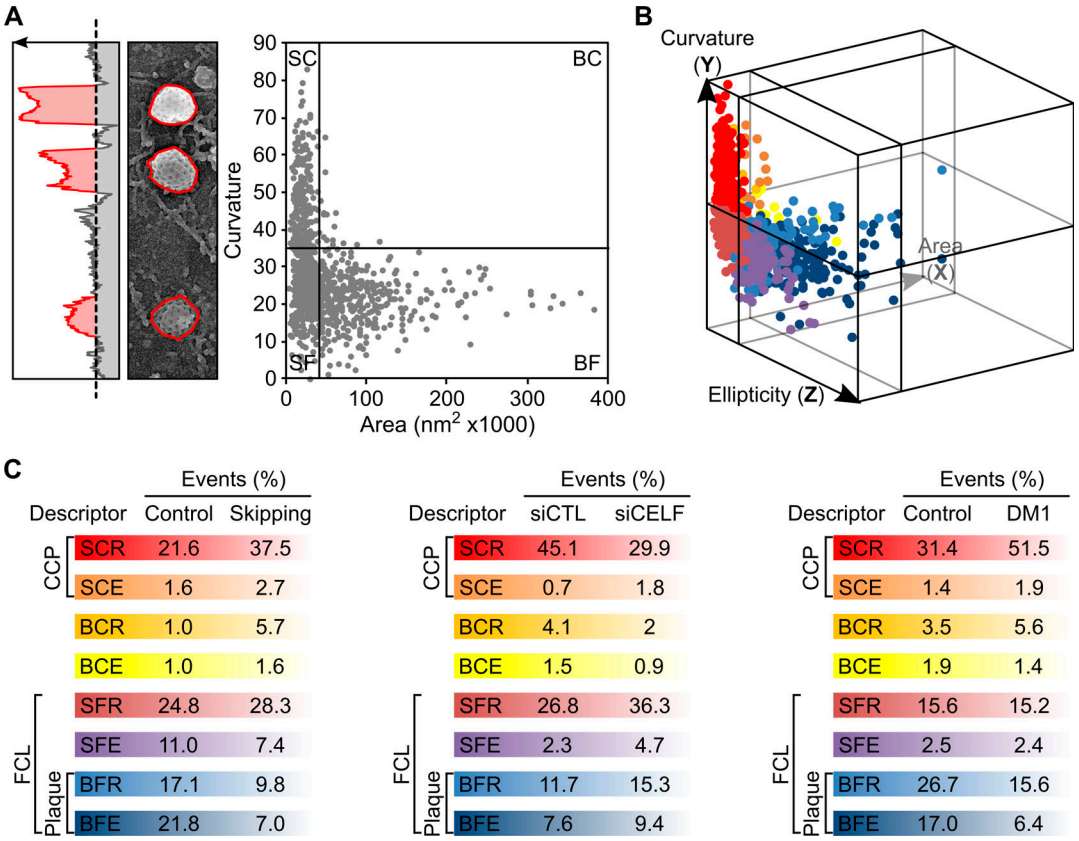


Figure S3. **Morphometric analysis of clathrin-coated structures on PREM images.** Related to Figs. 2 E, 4 C, and 5 D. **(A)** Illustration of the curvature quantification process on PREM images. Regions of interest (ROI) were manually traced around each clathrin structure (shown in red) as identified by their honeycomb appearance to measure the area of each structure. As electron opacity increases with clathrin structure budding, as shown here with three stages of CCP formation, the mean gray level of each ROI was quantified as a surrogate of structure curvature. The lighter gray shades correspond to spherical pits on top of the y curvature axis. Each clathrin structure was plotted over an x-y graph with area on the x axis and curvature on the y axis. Two cutoff thresholds were applied to classify objects into four categories: small and curved (SC), which corresponds to CCPs; big and curved (BC); and two FCL categories with small and flat (SF) structures and big and flat (BF) clathrin plaques. **(B)** Quantification of clathrin structure's relative frequencies in finer subcategories, including the ellipticity parameter. Clathrin structure ellipticity was used to further spread the previous graph (A) over a z axis in order to subclassify events as eight spaces formed by the intersection of three threshold planes. An arbitrary color was given to each of the eight spaces for distinction following the color code of descriptor categories in C. **(C)** Clathrin structure's relative frequencies according to the eight subcategories. These three columns of data present a finer morphometric quantification of experiments presented in Fig. 2 E, Fig. 3 C, and Fig. 5 F, respectively, with individual colors and three-letter descriptors for each clathrin structure subcategory. Descriptors correspond to the two-letter categories presented in A, each subdivided in two with the addition of a third letter (R for round or E for elliptical); thus, plaques defined as big and flat (BF) are now also described as round (BFR) or elliptical (BFE). siCTL, control siRNA; siCELF, CELF siRNA.

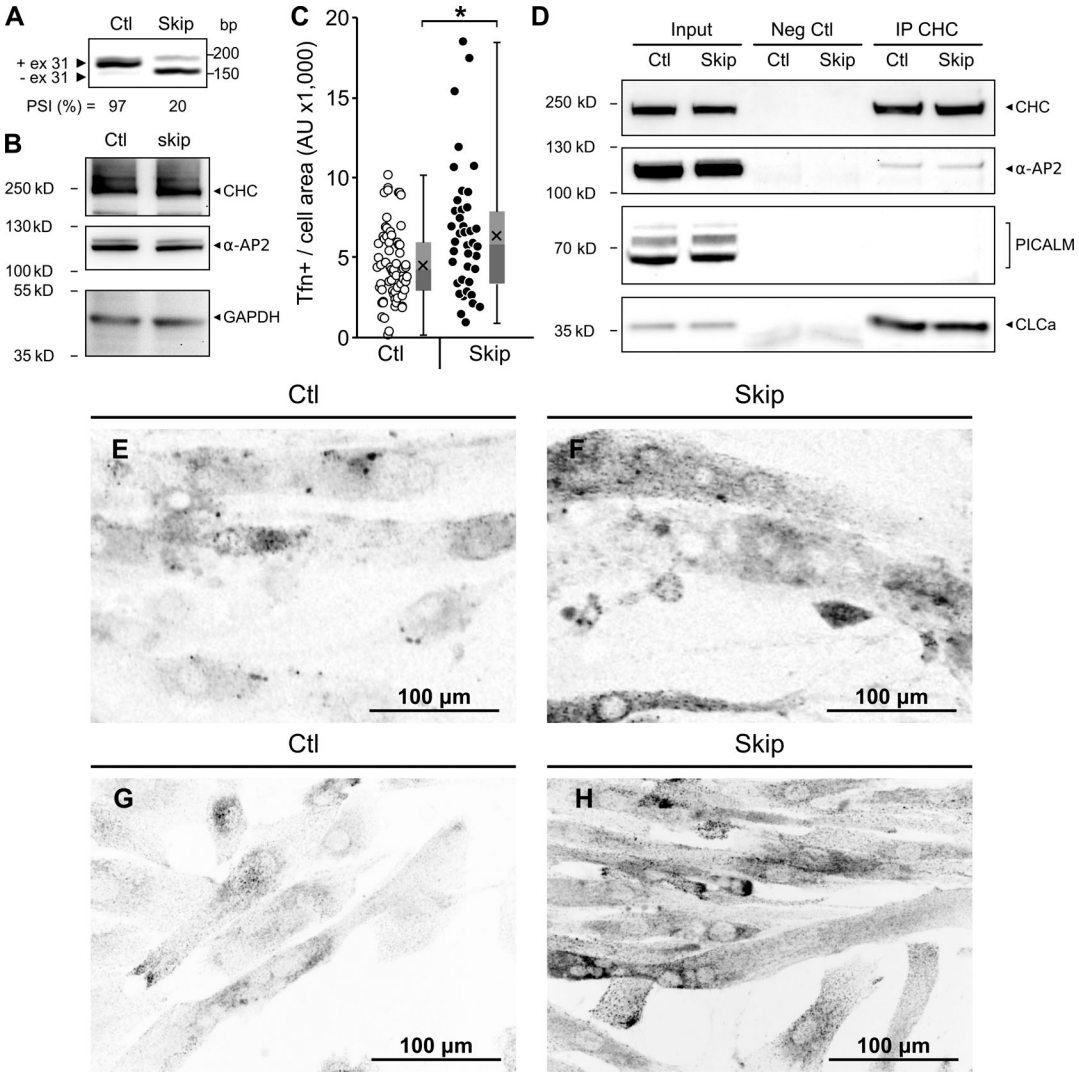


Figure S4. ***Cltc*-ex31 in vitro skipping in murine myotubes.** Related to Fig. 2. **(A–C)** Exon skipping was induced by AAV-U7-CLTCex31 vector transduction on 5-d differentiated mouse myotubes, followed by analysis 7 d later. **(A)** RT-PCR of *Cltc*-ex31 splicing. **(B and C)** Western blot and transferrin uptake assay from *Cltc*-ex31 skipping in murine myotubes as described for human myotubes in Fig. 2, B and H. Transferrin assay: Ctl, $n = 70$; Skip, $n = 42$; *, $P \leq 0.05$. Box plots show median extended from the 25th to 75th percentiles, minimum and maximum data point whiskers, and average cross. **(D)** Immunoprecipitation of CHC from 2-d differentiated C2C12 myotubes transduced or not by AAV-U7-CLTCex31 for 5 d. From left to right: 8% lysate inputs, immunoprecipitates with a nonrelevant antibody (Neg CTL), and CHC immunoprecipitates (IP CHC). CHC immunoblotting and coimmunoprecipitated α-AP2 and CLCa are indicated on the right. **(E and F)** Representative images corresponding to murine myotube transferrin uptakes quantified in C. **(G and H)** Representative images corresponding to human myotube transferrin uptakes quantified in Fig. 2 H. AU, arbitrary unit; Tfn, fluorescent transferrin.

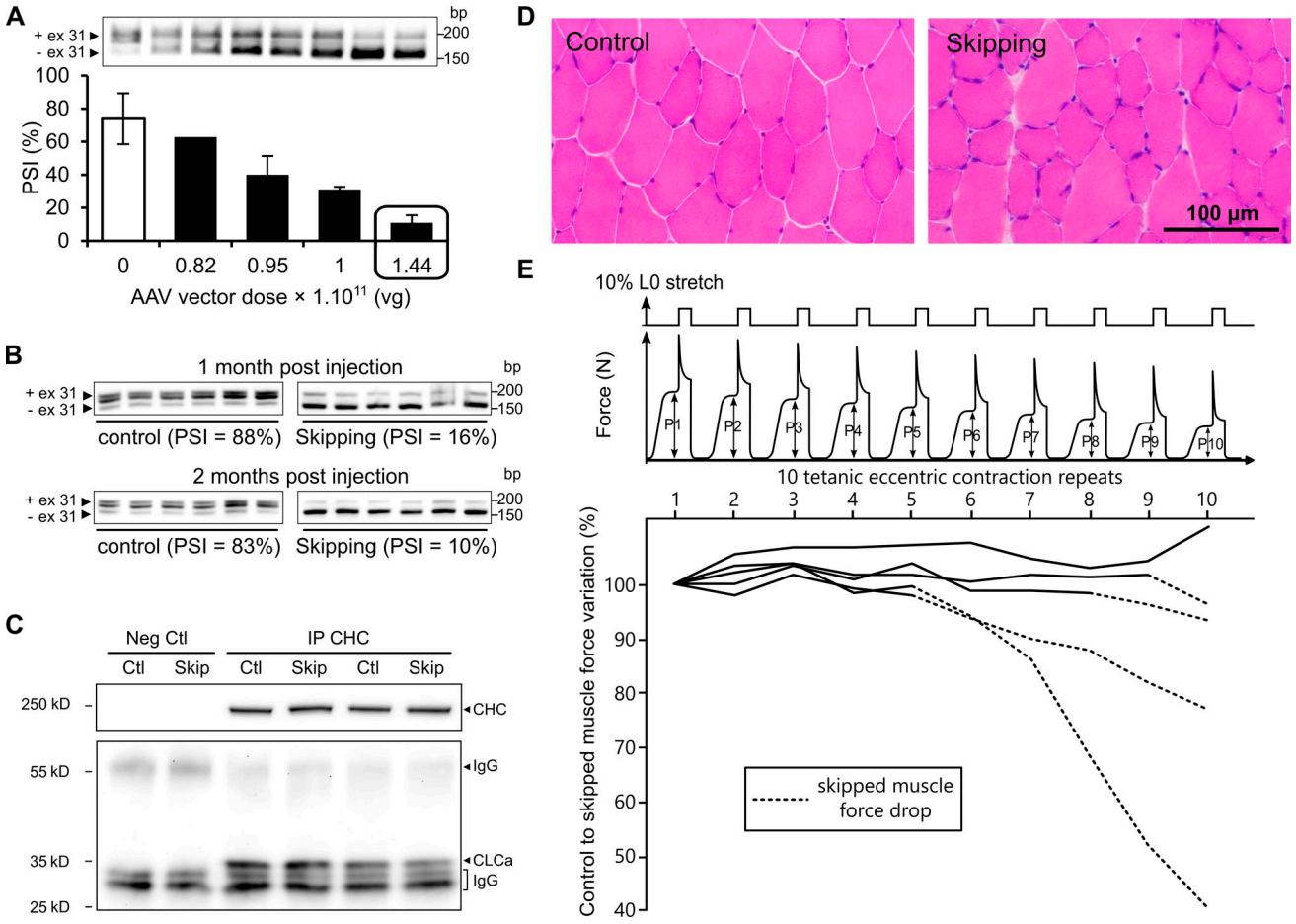


Figure S5. **In vivo exon skipping protocol validation and supplementary histological and functional data.** Related to Fig. 6. **(A)** RT-PCR validation of in vivo muscle exon skipping dose–response 1 mo PI. Representative *Cltc*-ex31 RT-PCR electrophoresis on top, with PSI quantifications below; the white bar corresponds to the average PSI from control saline-injected contralateral TA muscles, and the black bars to increasing AAV dosage ($n$ = 1 or 2 mice per dose). The optimal treatment dose used for Fig. 6 experiment is circled. Error bars correspond to SD. **(B)** RT-PCR *Cltc*-ex31 skipping validation in the TA of animals undergoing the optimal treatment 1 or 2 mo after administration compared with control saline-treated contralateral TA muscle (1-mo panels and 2-mo panels come from the same gels). **(C)** Immunoprecipitation of CHC from control saline-injected TA (Ctl) or AAV-U7-CLTCex31 injected TA muscle (Skip). From left to right: immunoprecipitates with a nonrelevant antibody (Neg Ctl) and CHC immunoprecipitates (IP CHC). CHC immunoblotting and coimmunoprecipitated CLCa are indicated on the right, along with IgG input. **(D)** Representative hematoxylin and eosin staining of protocol TA muscle transversal sections 1-mo PI. **(E)** Ratio of control to skipped muscle maximal tetanic force obtained in 10 successive eccentric contractions ($n$ = 5 mice) at 2 mo PI. When the force developed by the skipped muscle is lower than the one in the contralateral muscle, the curve is shown as a dashed line. Top: schematic representation of a typical myogram tracing.